

Article

Efficient Photocatalytic Degradation of Gaseous Benzene and Toluene over Novel Hybrid PIL@TiO₂/m-GO Composites

Shayeste Shajari ¹, Elaheh Kowsari ^{1,*}, Naemeh Seifvand ¹, Farshad Boorboor Ajdari ², Amutha Chinnappan ³, Seeram Ramakrishna ^{3,*}, Gopalan Saianand ⁴, Mohammad Dashti Najafi ¹, Vahid Haddadi-Asl ⁵ and Soheil Abdpour ¹

¹ Department of Chemistry, Amirkabir University of Technology, Tehran 1591634311, Iran; shayeste.shajari@gmail.com (S.S.); n_seifvand@yahoo.com (N.S.); mdn5310@gmail.com (M.D.N.); s66.abdpour@gmail.com (S.A.)

² Department of Applied Chemistry, Faculty of Chemistry, University of Kashan, Kashan 8731753153, Iran; frashd@gmail.com

³ Center for Nanofibers and Nanotechnology, Department of Mechanical Engineering, National University of Singapore, Singapore 119260, Singapore; maggieicaster@gmail.com

⁴ Global Center for Environmental Remediation (GCER), The University of Newcastle, Callaghan, NSW 2308, Australia; SaiAnand.Gopalan@newcastle.edu.au

⁵ Department of Polymer Engineering and Color Technology, Amirkabir University of Technology, Hafez Avenue, No. 424, Tehran 1591634311, Iran; haddadi@aut.ac.ir

* Correspondence: kowsarie@aut.ac.ir (E.K.); seeram@nus.edu.sg (S.R.)

Abstract: In this work, the PIL (poly ionic liquid)@TiO₂ composite was designed with two polymerized ionic liquid concentrations (low and high) and evaluated for pollutant degradation activity for benzene and toluene. The results showed that PIL (low)@TiO₂ composite was more active than PIL (high)@TiO₂ composites. The photodegradation rate of benzene and toluene pollutants by PIL (low)@TiO₂ and PIL (high)@TiO₂ composites was obtained as 86% and 74%, and 59% and 46%, respectively, under optimized conditions. The bandgap of TiO₂ was markedly lowered (3.2 eV to 2.2 eV) due to the formation of PIL (low)@TiO₂ composite. Besides, graphene oxide (GO) was used to grow the nano-photocatalysts' specific surface area. The as-synthesized PIL (low)@TiO₂@GO composite showed higher efficiency for benzene and toluene degradation which corresponds to 91% and 83%, respectively. The resultant novel hybrid photocatalyst (PIL@TiO₂/m-GO) was prepared and appropriately characterized for their microstructural, morphology, and catalytic properties. Among the studied photocatalysts, the PIL (low)@TiO₂@m-GO composite exhibits the highest activity in the degradation of benzene (97%) and toluene (97%). The ultimate bandgap of the composite reached 2.1 eV. Our results showed that the as-prepared composites hold an essential role for future considerations over organic pollutants.

Keywords: photocatalysis; poly ionic liquids; titanium dioxide; graphene oxide; gaseous benzene



Citation: Shajari, S.; Kowsari, E.; Seifvand, N.; Boorboor Ajdari, F.; Chinnappan, A.; Ramakrishna, S.; Saianand, G.; Dashti Najafi, M.; Haddadi-Asl, V.; Abdpour, S. Efficient Photocatalytic Degradation of Gaseous Benzene and Toluene over Novel Hybrid PIL@TiO₂/m-GO Composites. *Catalysts* **2021**, *11*, 126. <https://doi.org/10.3390/catal11010126>

Received: 11 November 2020

Accepted: 11 January 2021

Published: 15 January 2021

Publisher's Note: MDPI stays neutral with regard to jurisdictional claims in published maps and institutional affiliations.



Copyright: © 2021 by the authors. Licensee MDPI, Basel, Switzerland. This article is an open access article distributed under the terms and conditions of the Creative Commons Attribution (CC BY) license (<https://creativecommons.org/licenses/by/4.0/>).

1. Introduction

With the advent of the industry and the increased use of fossil fuels and processed materials from the fossil fuel source, we are faced with the phenomenon of air pollution [1]. Air pollution has seriously affected the environment and the health of humans and other organisms [2]. Common air pollutants include carbon monoxide (CO), nitrogen oxides (NO_x), suspended particles, and volatile organic compounds [3,4]. Volatile organic compounds (VOCs), as toxic compounds, cause genetic mutations, leukemia, and various types of cancers. They also affect organs such as the lungs, skin, and brain, and are known to be one of Alzheimer's agents [5–7]. The epidemiological studies showed significant concerns over the relationship between severe myelogenous leukemia and benzene exposure (as one of the dangerous VOCs). Inhalation is the most primary procedure of exposing benzene molecules that exists in outside air. They can even penetrate the body through skin contact,

which is usually accelerated by touch with petroleum and petrochemical products; however, it is less common due to quick evaporation [8,9]. The removal of benzene and toluene using a photocatalytic degradation technique is an efficient and cost-effective process [10–12]. The photocatalytic oxidation of VOCs comprises a chain of step-by-step reactions. The photocatalytic reaction rate is a criterion for assessing the efficiency of a photocatalyst in the elimination of volatile organic compounds [13–15]. Temperature, inactivity, pollutant concentration, relative humidity, and light intensity are challenging determinants toward controlling photocatalytic behavior or performance. Photocatalytic lifetime is an important parameter for the actual use of domestic pollutants removal. Deactivation also needs to be considered; it occurs due to the accumulation of oxidized partial intermediates occupying active sites at the photocatalyst level [16,17]. There exists a strong desire for the coupling of photoexcited electron–hole pairs, and the comparatively wide bandgap contributes to the lack of visible light absorption [18]. Some techniques such as doping, interconnecting with other semiconductors, metal oxide, and carbon materials have been proposed to increase the electron–hole pairs' existence and reduce the bandgap [19,20]. Reduced graphene oxide, as the electron acceptor and donor, can prevent electron–cavity recombination [21,22]. Reduced graphene oxide is also a supporting substrate for manganese complexes. Benzene can be used as a ligand in complex structures [23]. The overlapping of π – π connections between benzene and its aromatic nature leads to surface absorption [24,25]. Ionic liquids, as the reaction medium toward the preparation of inorganic nanoparticles, have mainly been used due to the unique properties as high intrinsic load and ionic liquids' polarity to create spatial and electrostatic stability for nanoparticles. Moreover, they posed an excellent template for the preparation of porous nanomaterials [26,27]. Besides, utilizing ionic liquid in the synthesis process will reduce the number of useful parameters on the reaction and make the mechanism more understandable. [28,29]. It allows the reaction parameters to be well adjusted. As ionic liquids have low surface tension, the morphological control of nanoparticles is guaranteed in an ionic liquid environment. Ionic liquids can form an electrostatic shell around nanoparticles due to the presence of cations and anions, which prevents the accumulation of nanoparticles [30–32]. These compounds are non-volatile, non-toxic, and non-corrosive. When used as a catalyst for this material, surface modification increases selectivity and reactivity. Solid polymer electrolytes (SPEs) built from a polymer matrix and a salt. PIL is known as poly-electrolyte [33,34]. Electrolytes are compounds that like to be separated poly-electrolytes are polymers that do the same thing. Normal molecules without polymer loads are twisted, but when the polymer chain is full of negative loads (which repel each other), it cannot be integrated into itself. Therefore, the chain is drawn and then occupies more space. As a catalyst must have a significant active surface to absorb more reagent, increasing the level of the polymeric field provides more chance and prevents nanoparticles from accumulation [35,36]. This research attempts to reduce the effects of benzene and toluene by converting them into non-toxic benign materials.

The photocatalytic degradation can occur at band structures, in which oxidation and reduction are, respectively, carried out at valence band (VB) and conduction band (CB). As illustrated in Figure 1, efficient energy-absorbing of photons by poly ionic liquid, leads to electron exciting and moving from the highest occupied molecular orbital (HOMO) to the lowest unoccupied molecular orbital (LUMO). Both VB and CB experienced growth in energy levels and TiO_2 enjoyed a lowered bandgap due to an intimate interaction between TiO_2 and poly ionic liquid. The excited electrons would be carried to the TiO_2 's conducting band, departing holes in the valence band due to the electrostatic attraction between the electrons and PIL cations (positively charged) [37]. Growing TiO_2 's photocatalytic performance and suppressing electron–hole recombination is in direct agreement with accepting electrons of m-GO from TiO_2 and shuttling the negative charges from TiO_2 within the graphitic sp^2 -hybridized aromatic system [38].

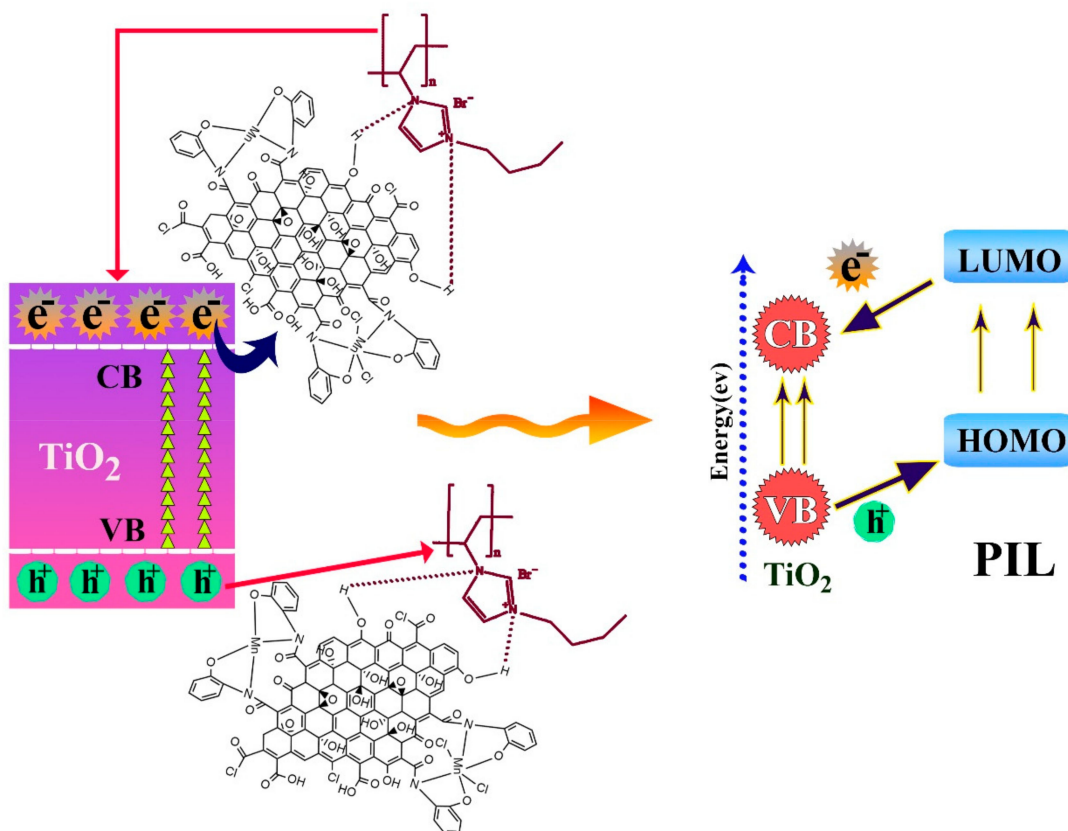


Figure 1. Schematic illustrating photocatalytic degradation with the help of band structures.

MengWang et al. and coworkers were reported beyond 90% degrading yields for benzene and toluene during 1 and 2 h, respectively, by CDs/CdS-TiO₂ nanocomposites. While the CDs/CdS-TiO₂'s bandgap hit the point of 2.28 eV [39], our newly synthesized PIL(low)@TiO₂@m-GO nanocomposite obtained a high degradation efficiency of 97% for benzene and toluene within 24 min. The bandgap energy of PIL(low)@TiO₂@m-GO was estimated as 2.1 eV, in which the modified graphene oxide (m-GO) efficiently contributed to electron-hole recombination prevention.

Here, we prepared pure titanium dioxide (TiO₂) through the sol-gel approach [40,41]. The DRS was then performed on titanium dioxide to consider the ultraviolet (UV) and visible light absorption efficiency. We considered the activity of TiO₂ for observing the photocatalytic degradation of pollutants. Then, the PIL@TiO₂ composite was designed with two polymerized ionic liquid concentrations, both of which were identified by DRS and XRD tests and evaluated for pollutant degradation activity. The results showed that PIL (low)@TiO₂ composite was more active than PIL (high)@TiO₂ composite. TEM test was performed on PIL (low)@TiO₂ composite, where the coating of titanium dioxide nanoparticles by polymer chain is well visible. Degradation of benzene and toluene pollutants by PIL (low)@TiO₂ and PIL (high)@TiO₂ composites was obtained as (86% and 74%) and (59% and 46%), respectively. The titanium dioxide enjoyed a considerable measure of reduction bandgap (3.2 to 2.2 eV) due to the formation of PIL (low)@TiO₂ composite.

The as-synthesized PIL (low)@TiO₂@GO composite had higher activity in benzene and toluene degradation of 91% and 83%, respectively. By converting carboxyl groups to acyl chloride and then reacting with amines, some promising ligands appeared to place manganese-based complexes on the GO surface. Furthermore, modified graphene oxide (m-GO) was characterized by XPS, XRD, Raman, TEM, and FE-SEM tests. The PIL (low)@TiO₂@m-GO composite showed the most promising performance toward the benzene and toluene degradation. The ultimate bandgap of the composite reached 2.1 eV. Our innovation is to reduce the bandgap of TiO₂. The reported bandgap for TiO₂ is 3.2 eV. In this study,

the amount of bandgap was reduced to 2.1 eV by the composite of PIL(low)@TiO₂@m-GO. Another point of interest in this study is the relative concentration of contaminants associated with the radiation distribution period. The relative concentration of pollutants to the distribution of irradiation time shows that the composite of PIL(low)@TiO₂@m-GO destroyed 97% of the pollutants within 24 min.

2. Analyzing the Data and Results

2.1. Characterization

2.1.1. XRD Patterns

The XRD patterns of all samples were recorded and discussed for confirming the presence of the functional materials and as-prepared materials. The higher peak intensity symbolizes a higher amount of compound in the sample. The presence of particles was characterized by appeared angles corresponding to that material's peaks. TiO₂ nanoparticles were observed in the anatase phase [42,43]. In Figure 2a, the XRD pattern of TiO₂ shows a peak at 25° that corresponds to (101) with a d-spacing of 3.4 Å°. This spectrum exhibits orientations at 38.2°, 48.6°, 57.6°, and 63.2° that attributes to (004), (002), (105), and (204), respectively [44,45]. TiO₂ was blended with different concentrations of the PIL. Figure 2a indicates a composite with a lower concentration of PIL, made an amorphous structure rely on the XRD of pure TiO₂ [46]. The appeared peaks at 22.6°, 32.07°, 45.46°, and 56.7° are attributed to the anatase phase of TiO₂. By fabricating pure TiO₂ in the composite, the peak of TiO₂ shifted to lower angles. It can be attributed to an increase in the crystal size in ionic liquid [47,48]. In the composite with a higher concentration of ionic liquid, the crystal size was expanded due to the high amount of polyionic liquid.

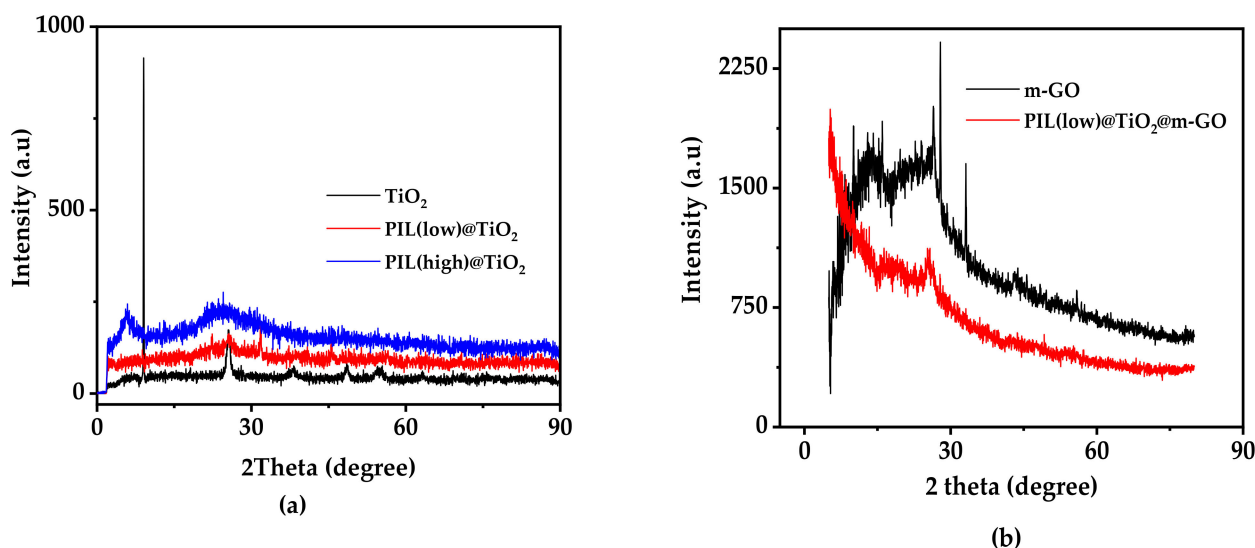


Figure 2. XRD pattern of (a) TiO₂, PIL(low)@TiO₂, PIL(high)@TiO₂, (b) m-GO, and PIL(low)@TiO₂@m-GO.

Figure 2b shows two obvious shifted peaks at 19° and 26° with reduced d-spacing (4.63 Å°) for modified graphene oxide (m-GO), indicating successful functioning of Mn complex on the GO surface [49–51]. The XRD of PIL(low)@TiO₂@m-GO (Figure 2b), compares the appeared peaks of PIL(low)@TiO₂@m-GO and m-GO, where TiO₂ and PIL give low peaks different functional on m-GO. The XRD of the PIL(low)@TiO₂@m-GO with decreased layers distance, is evidence for the successful formation of composites.

2.1.2. FESEM and TEM Images

TEM of m-GO: Based on the TEM image (Figure 3a,b), the surface of graphene oxide is surrounded by functional groups, which own darker points [52–54].

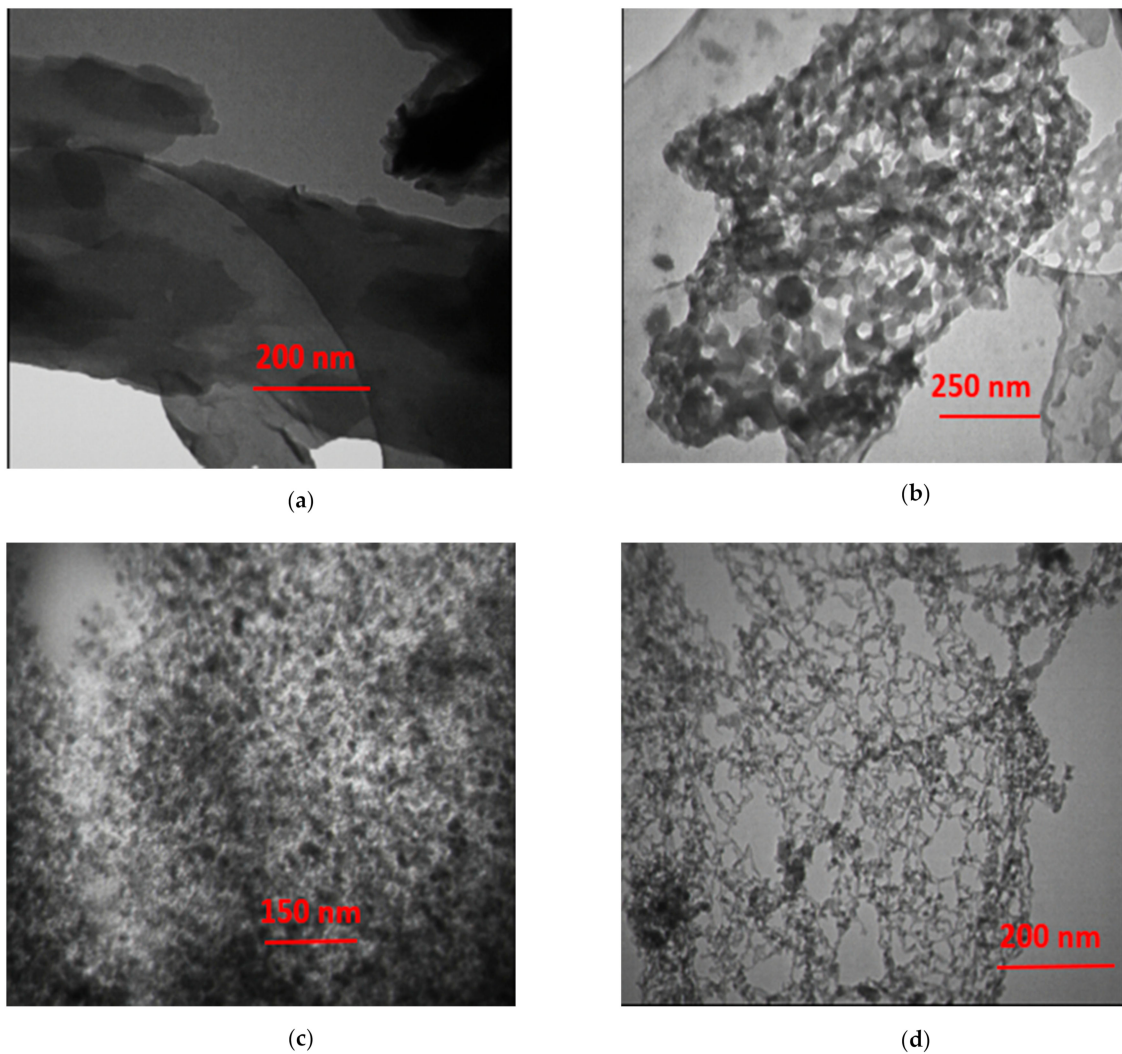


Figure 3. TEM images from different angles of m-GO (a,b) and PIL(low)@TiO₂ (c,d).

TEM of PIL(low)@TiO₂: The transmission electron microscopy (TEM) of PIL(low)@TiO₂ (shown in Figure 3c) indicates the homogeneous distribution of nanoparticles. It can attribute to the well-dispersed process. Moreover, covering titanium dioxide nanoparticles with polymer chains is clearly shown in Figure 3c,d.

SEM of m-GO: The SEM images clearly show the three-dimensional graphene oxide sheet, which possesses a structure similar to a sponge. The accumulation of layers in some areas can be attributed to operational groups (Figure 4) [55,56]. Due to each element's unique atomic structure, the energy generated by electron transfer between two layers with different energies is shown in the graph of EDX (Figure S1).

SEM of PIL(low)@TiO₂@m-GO: Composite morphology shows graphene layers are coated with polymer chains that surround titanium dioxide nanoparticles (Figure 5).

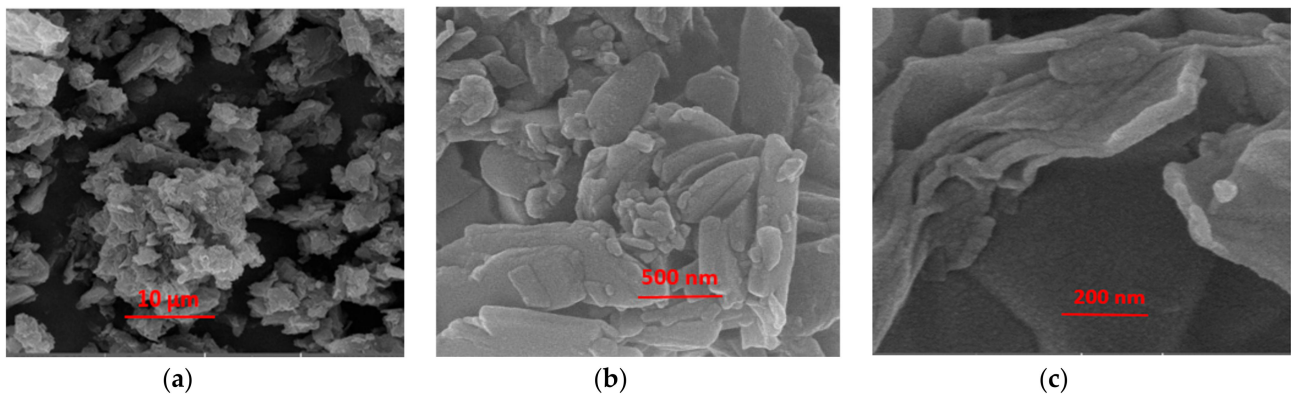


Figure 4. Field emission scanning electron microscopy (FESEM) pictures with different magnifications of m-GO (a–c).

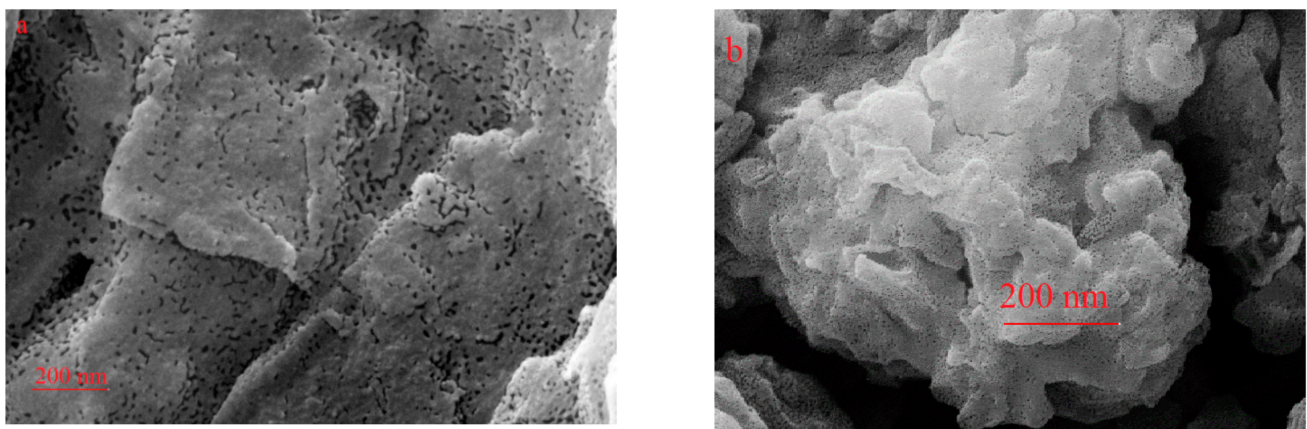


Figure 5. FESEM pictures with different magnifications of PIL(low)@TiO₂@m-GO, (a) chain of poly ionic Liquid on m-GO layers; (b) m-Go layers coated with polymer chains from another view.

2.1.3. X-Ray Photoelectron Spectroscopy (XPS)

The XPS results for manganese functionalized graphene oxide (m-GO) deconvolution are indicated in Figure 6. The results for m-GO show the presence of carbon (C1s 84.68%), oxygen (O 1s 10.07%), nitrogen (N 1s 3.17%), Cl (2p 1.59%), and manganese (Mn 2p 0.49%) (Figure 6a). The deconvolution peak of C1s for the m-GO (Figure 6b) also exhibited binding energies of 284.7, 284.9, 285.9, 286.9, 288.1, and 289.02 eV with a mean consistent FWHM of 1.21 eV, due to C–C, C–OH, C–N, C=O, C(O)N, C(O)O groups [57,58]. The Cl 2p peak arises from two major parts: the position of Cl 2p_{3/2} at 200.2 eV and Cl 2p_{1/2} at 201.5 eV (Figure 6c) [59]. As seen in Figure 6d, two kinds of nitrogen bonds with high-resolution N 1s spectrum, including N–C=O and N–C, are displayed at 400.2 eV and 398.5 eV, respectively [60,61]. Similarly, in Figure 6e, the O 1s binding energies showed by the untreated substrate at 529.7, 530.2, and 531.9 eV were assigned to C=O, O–H, and C(O)O, respectively [62]. As shown in the high-resolution Mn 2p range (Figure 6f), two pairs of spin-orbit resolved peaks related to Mn 2p_{3/2} are located at 640.1 and 651.7 eV, with a spin-energy separation value of 11.6 eV [63]. The peaks of Mn⁴⁺ 2p_{1/2}, Mn⁴⁺ 2p_{3/2}, Mn²⁺ 2p_{1/2} and Mn²⁺ 2p_{3/2} are centered at 656.2, 643.5, 651.8, and 640.2, respectively [64].

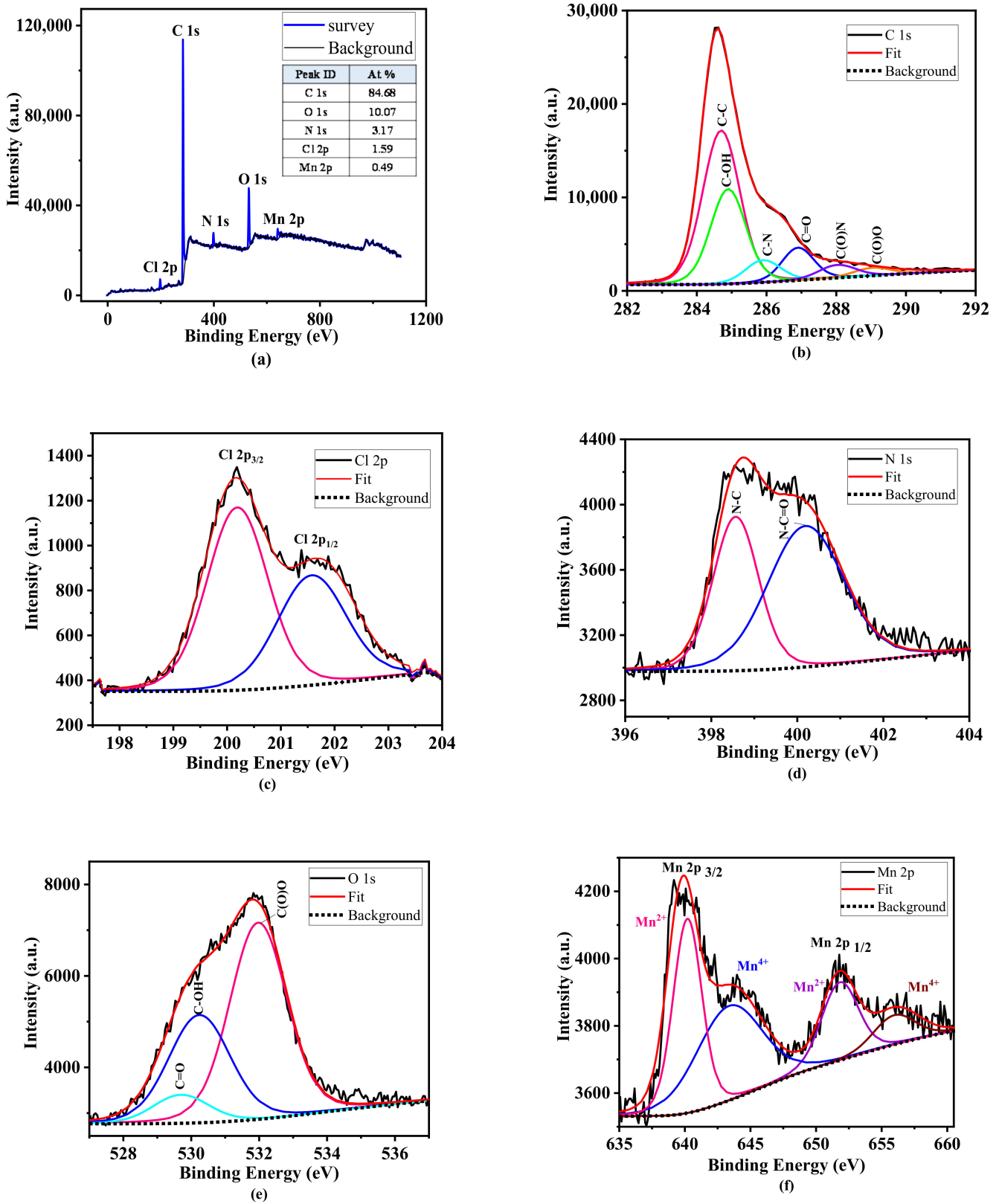


Figure 6. XPS spectroscopy (XPS) for manganese functionalized graphene oxide (m-GO), survey (a), xps of C 1s (b), Cl 2p (c), N 1s (d), O 1s (e), and Mn 2p (f).

2.1.4. Spectroscopy Results for FTIR

The FTIR plot of m-GO is shown in Figure 7. In the IR spectrum, it is possible to identify stretch vibrations characteristics of each unique bond. At 3433.21 cm^{-1} , there is the O–H stretching band. The peak at 2922 cm^{-1} is assigned to C–H (alkane). There is a weak peak at 2074 cm^{-1} can be attributed to tropospheric ozone [51,65–68]. The other peak presents at 1629 cm^{-1} confirm the presence of C=O (amide) that mentions the excellent process of graphene oxide's operationalization that is also confirmed in the XRD chart. The existence of a peak at 1572 cm^{-1} is related to the C=C ring. The spectra showed two weak peaks at 1406 cm^{-1} corresponding to CH₂ deformation. The peak at 1171 cm^{-1} and 1020 cm^{-1} is attributed to C–O–C and C–N, respectively. The range is from 753 cm^{-1} to 950 cm^{-1} , which confirms CH bending and ring puckering [69]. The courier in 578 cm^{-1} represents the presence of the Mn–O bond [70].

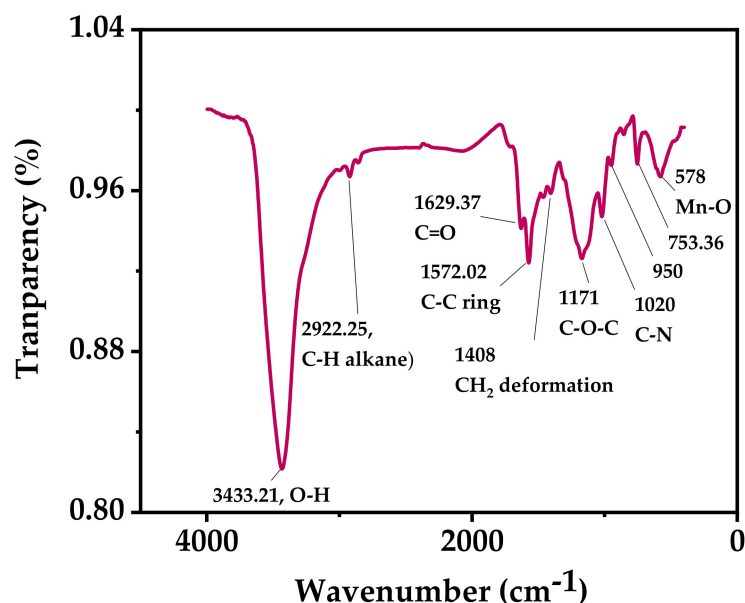


Figure 7. FT-IR spectrum of m-GO.

2.1.5. Raman Spectra

As observed in the Raman spectra of m-GO (Figure S2), the documented G band (@ 1550 cm^{-1}) indicates vibrations of sp^2 carbon atoms and E_{2g} symmetry, and the latter peak of D band (@ 1337 cm^{-1}) can be ascribed to sp^3 defects and A_{1g} symmetry. The structural disorder was evaluated by I_D/I_G ratio measures. Another significant feature in the Raman spectra of m-GO is an I_D band at 2680 cm^{-1} , derived from the stacking nature of treated layers of graphene oxide. A decrease in the I_D band intensity is attributed to the breaking of the stacking order. According to the spectrum, the peak is not visible at 2700 cm^{-1} , validating the lack of the accumulated layers in the Raman spectra of m-GO (Figure S2). [71–73]. The ratio of D-band to G-band intensity I_D/I_G was applied to measure structural disorder. As the I_D/I_G ratio increases, structural disruption increases. Increasing the I_D/I_G ratio in operationalized graphene oxide (0.99) to the I_D/I_G ratio graphene oxide (0.91) proves the lattice structure's disruption. The presence of peaks at (560 cm^{-1} , 992 cm^{-1}) refers to the Mn–O band, and peak at 358 cm^{-1} attributes to the Mn–Cl band [74,75].

2.1.6. Band Gap Determination and UV–Vis Spectra

The optical absorption was considered by filed data of UV–Vis DRS spectra of PIL(high)@TiO₂, PIL(low)@TiO₂, and PIL(low)@TiO₂@m-GO (Figure S3). Table 1 summarizes the results of band gap.

Table 1. Band gap of different photocatalysts.

Photocatalyst	Band Gap (ev)
TiO ₂	3.2
PIL(high)/TiO ₂	2.53
PIL(low)/TiO ₂	2.15
PIL(low)/TiO ₂ /m-GO	2.1

The TiO₂ band gap was reported as 3.2 eV [76]. In the DRS spectra of PIL(high)@TiO₂, intense absorption in the ultraviolet region was observed due to the sizeable TiO₂ bandgap. The calculated band gap for PIL(high)@TiO₂ is 2.53 eV. The UV–Vis DRS spectra of PIL(low)@TiO₂ shows increased efficiency of absorption in the ultraviolet region and poor absorption in the visible region’s lower wavelengths. The measured band gap of PIL(low)@TiO₂ is 2.2 eV. The UV–Vis DRS spectra of PIL(low)@TiO₂@m-GO showed strong absorption in the ultraviolet and visible region. The reported bandgap for PIL(low)@TiO₂@m-GO is 2.1 eV. The reduction of the final composite band gap shows the PIL’s effect and graphene oxide (Figure S4).

2.2. Photocatalytic Activity towards Degradation of Benzene and Toluene

2.2.1. Evaluating the Photocatalytic Results

The photocatalytic yield of nanomaterials, based on the benzene and toluene degrading (Figure 8), was carried out. The shape shows the relative concentrations (C/C_0) of benzene and toluene relative to the different nanostructures’ radiation time distribution. C shows the concentration of contaminants at the time of radiation (t) and C_0 initial concentrations before radiation. It was observed that the pollutants’ concentration decreased with increasing radiation time for all nanostructures, which shows the photocatalytic properties of nanostructures in the visible light. The initial concentration of VOCs, used in this study, was 50 ppm. Pollutant removal was done in 32 min (8 min in the dark and 24 min under UV–visible light). Regarding the dark region, only small amounts of both benzene and toluene were removed by photocatalytic activity, attributed to photocatalysts’ adsorption. The highest adsorption in darkness was recorded by PIL(low)/TiO₂/m-GO nanocomposite, which shows a significant role of graphene oxide presence. According to the figure, 24% of destruction for toluene is observed by photocatalyst TiO₂ thin-film. As the composite PIL/TiO₂ was constructed in two ionic liquid concentrations, the photocatalytic activity of both samples was studied. The sample with more ionic liquid concentration had 46% toluene degradation, and the sample with less ionic liquid concentration had 74% toluene degradation. In the following, we dope a composite sample with a low concentration of ionic liquid/titanium dioxide with graphene oxide (PIL(low)/TiO₂/GO), which shows the destruction of 83% toluene within 24 min. If composite PIL(low)/TiO₂/m-GO is placed under light UV, 97% of toluene’s destruction is observed. The photocatalytic degradation of benzene, as well as the photocatalytic degradation of toluene, was investigated. The destruction was reported for TiO₂ thin-film 42%, PIL(high)@TiO₂ 59%, PIL (low)@TiO₂ 86%, PIL (low)@TiO₂/GO 91%, and PIL (low)@TiO₂/m-GO 97%. It can be concluded that with the improvement of photocatalyst properties, the rate of degradation of pollutants increases [43,75,77]. Error bars represent standard deviations on [pollutant]/[pollutant] (Figure 8).

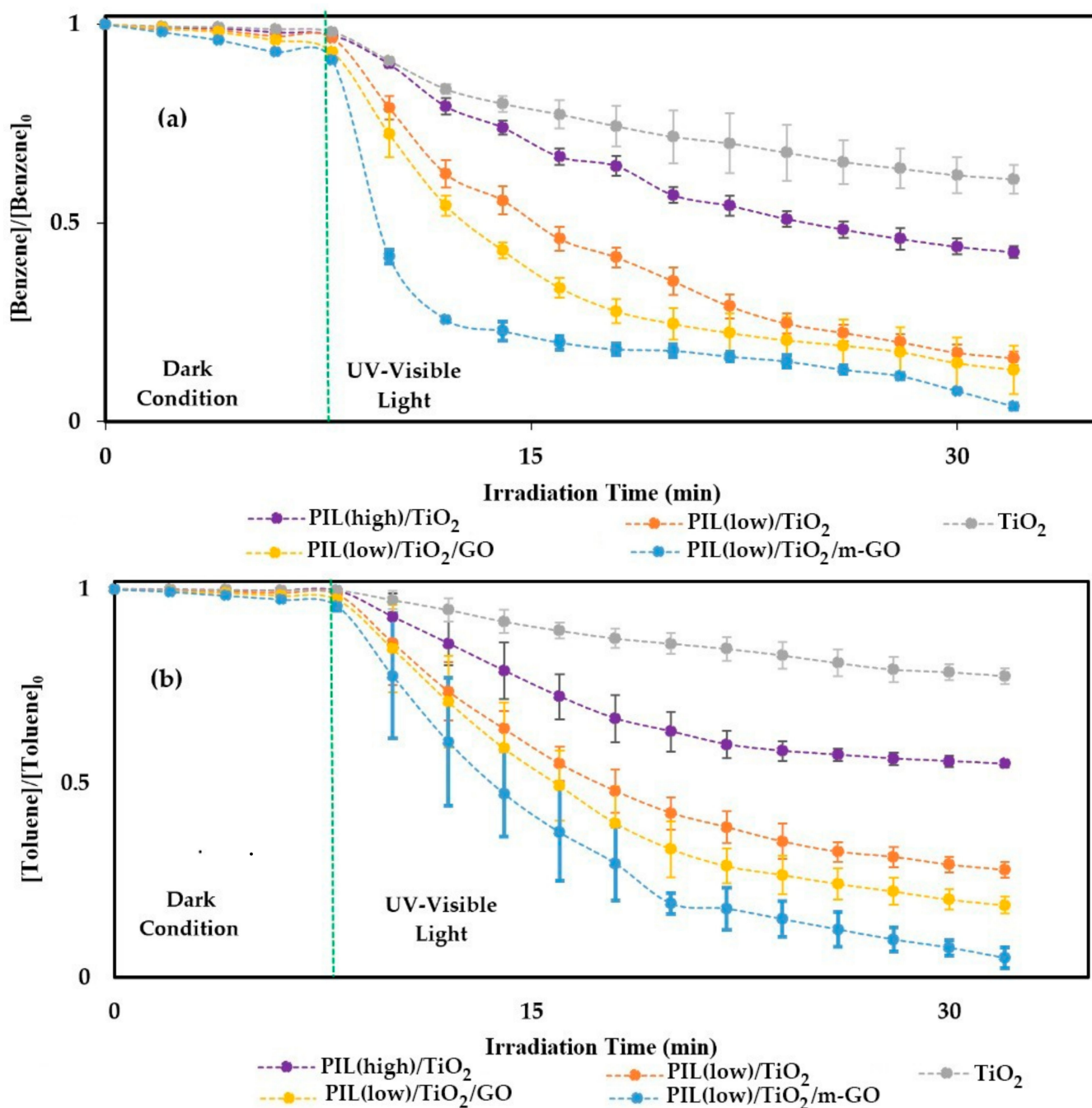


Figure 8. Photodegradation of (a) benzene and (b) toluene with irradiation time over five samples (first 8 min under dark and then 24 min under UV-visible radiation) of TiO₂, PIL(high)@TiO₂, PIL(low)@TiO₂, PIL(low)@TiO₂ (97 wt.%)/GO (3 wt.%) and PIL(low)@TiO₂(97 wt.%). /m-GO (3 wt.%).

The specific activities of TiO₂, PIL(high)/TiO₂, PIL(low)/TiO₂, PIL(low)/TiO₂/GO and PIL(low)/TiO₂/m-GO photocatalysts at the steady state of the reactions are reported in Table 2. The results show photocatalytic performance for degrading benzene and Toluene. Poly ionic liquid increases the activity of TiO₂, the activity was still much lower than PIL(low)/TiO₂/m-GO. The presence of functionalized graphene oxide increases TiO₂ activity [78,79].

Table 2. Specific catalytic activity of different photocatalysts for benzene and toluene.

Photocatalyst	Benzene	Toluene
	$\mu\text{mol. g}^{-1} \cdot \text{h}^{-1}$	$\mu\text{mol. g}^{-1} \cdot \text{h}^{-1}$
TiO ₂	0.7	1.9
PIL(high)/TiO ₂	0.98	3.64
PIL(low)/TiO ₂	1.43	5.85
PIL(low)/TiO ₂ /GO	1.52	6.59
PIL(low)/TiO ₂ /m-GO	1.62	7.67

2.2.2. Kinetic Studies of Benzene and Toluene Photocatalytic Degradation

Kinetic considerations were also studied over photocatalytic activity for benzene and toluene removal to achieve the scale-up perspective from the lab outcomes. A typical PF reactor (plug flow reactor) was employed, which ignored mass transport restrictions from the gas-to-solid phase to promote the model. Concerning the first-order reaction, the value of r_A (rate coefficient) is independent of the Q measure (flow rate). By fixing volume limits and concentration intergradations, can be calculated following Equations (1)–(3) are used for calculating the first-order equation.

$$Q C_A dt = Q (C_A + d C_A) dt + (r_A) dV dt \quad (1)$$

$$r_A = -dC_A/dt = K' C_A \quad (2)$$

$$\ln (C_{A0}/C_A) = K' t \quad (3)$$

where the signs represent

(C_{A0}): Initial pollutants concentrations,

(C_A): Final pollutants concentrations,

(K'): Rate constant of the first-order reaction, and

(t): Accommodation time.

The K' values were obtained by graphing $\ln(C_{A0}/C_A)$ values as a function of pollutants' photodegradation.

The line's angular coefficient and linear adjustment were respectively used to determine the K' and R^2 as kinetic parameters. A similar plan was utilized over measuring the second-order kinetics parameters, where K'' (equation constant) was measured through graphing $(1/C_A - 1/C_{A0})$ versus time (finding slope value). (Equations (4) and (5)) employing Equations (4) and (5):

$$r_A = -dC_A / dt = K'' C_A^2 \quad (4)$$

$$(1/ C_A - 1/ C_{A0}) = K'' t \quad (5)$$

degradation rate constant attributes to the slop of a liner plot of $\ln(C_{A0} / C_A)$ as a function of time. The nanocomposite sample has the highest K value and, therefore, the highest pollutant degradation rate. Each of the photocatalytic samples investigated the first- and second-order kinetics of pollutant degradation, and R^2 of each kinetic model was stated. The more considerable value of R^2 means the trusting kinetic model. PIL(low)/TiO₂/m-GO photocatalytic behavior for kinetics of the degradation of benzene molecules has not entirely matched the first second-order kinetic models, and seems it more complicated behavior of kinetics [76,80]. However, PIL(low)/TiO₂/m-GO was well matched with the first-order theory ($R^2 = 0/9705$). The plotted diagrams of kinetic data were drawn in Figure S5, and Table 3 summarizes the results of the kinetic data for benzene and toluene degradation.

Table 3. The kinetic data for benzene and toluene degradation.

Photocatalyst	Benzene Degradation Kinetic Data			
	First-order data		Second-order data	
	K' (min ⁻¹)	R ²	K'' [(ppmv) ⁻¹ .min ⁻¹]	R ²
TiO ₂	0/0279	0/9427	0/0007	0/9162
PIL(high)/TiO ₂	0/0425	0/972	0/0013	0/9932
PIL(low)/TiO ₂	0/0891	0/8415	0/0046	0/9518
PIL(low)/TiO ₂ /GO	0/1108	0/9333	0/0072	0/9476
PIL(low)/TiO ₂ /m-GO	0/136	0/6361	0/0133	0/5465
Photocatalyst	Toluene Degradation Kinetic Data			
	First-order data		Second-order data	
	K' (min ⁻¹)	R ²	K'' [(ppmv) ⁻¹ .min ⁻¹]	R ²
TiO ₂	0.013	0/9093	0/0003	0/9427
PIL(high)/TiO ₂	0/0328	0/7225	0/0009	0/8242
PIL(low)/TiO ₂	0/0659	0/8963	0/0025	0/9896
PIL(low)/TiO ₂ /GO	0/0879	0/8858	0/0043	0/9875
PIL(low)/TiO ₂ /m-GO	0/1425	0/9705	0/0153	0/7053

2.2.3. Photocatalytic Benzene and Toluene Degradation Mechanism

PIL(low)/TiO₂/m-GO acts with two radical mechanisms (by PIL@TiO₂) and absorption through the formation of composite a complex (Figure 9). Manganese is the central metal of the complex and benzene and toluene in the ligand's role. Graphene oxide as a conductive electric charge and an electron holding conductor through its π bonds play an essential role in bringing electrons to manganese ligands and performing radical mechanisms [81,82].

The radicals produced by TiO₂ cause photocatalyst oxidation and thus the destruction of pollutants. Besides, lateral products will be produced during this process that eventually converts to H₂O and CO₂. The radical mechanism of benzene degradation is indicated in Figure 10 [83]. Benzene, as a neutral ligand, forms the complex with metal. In benzene, carbons 1 and 4 have closer positions to the metal. In this structure, the aromatic state is slightly degraded, and the electrons are concentrated at a certain point. The aromatic state's degradation and weakening make it possible to bond manganese to benzene [84,85]. When there is an atom of metal, finally, two benzene molecules can bond. This description is also valid for the toluene.

TiO₂ produces a unique electron transfer process that can promote the separation of the hole–electron pairs to grow photocatalyst activity. Functionalized graphene (m-GO) owns a strong adsorption capacity and a large surface; therefore, it intensifies the adsorption ability of TiO₂@PIL@m-GO. Furthermore, m-GO can work as an electron acceptor due to its two-dimensional π -conjugation structure.

Using m-GO contributes to creating the valence band and conduction band, including highest occupied molecular orbital (HOMO) and lowest unoccupied molecular orbital (LUMO) bands, forming sub-layer energy (π orbital) further down than the TiO₂'s conduction zone (d orbital). Thus, the activation of the catalyst was performed under its original wavenumber radiation. Besides, the long-chain PILs contribute to improved conductivity. The excited electrons of TiO₂ nanoparticles can quickly transfer from the conduction band of TiO₂ to m-GO. Thus, photogenerated charge carriers' recombination is reduced, and more reactive species will exist for the pollutants' photodegradation.

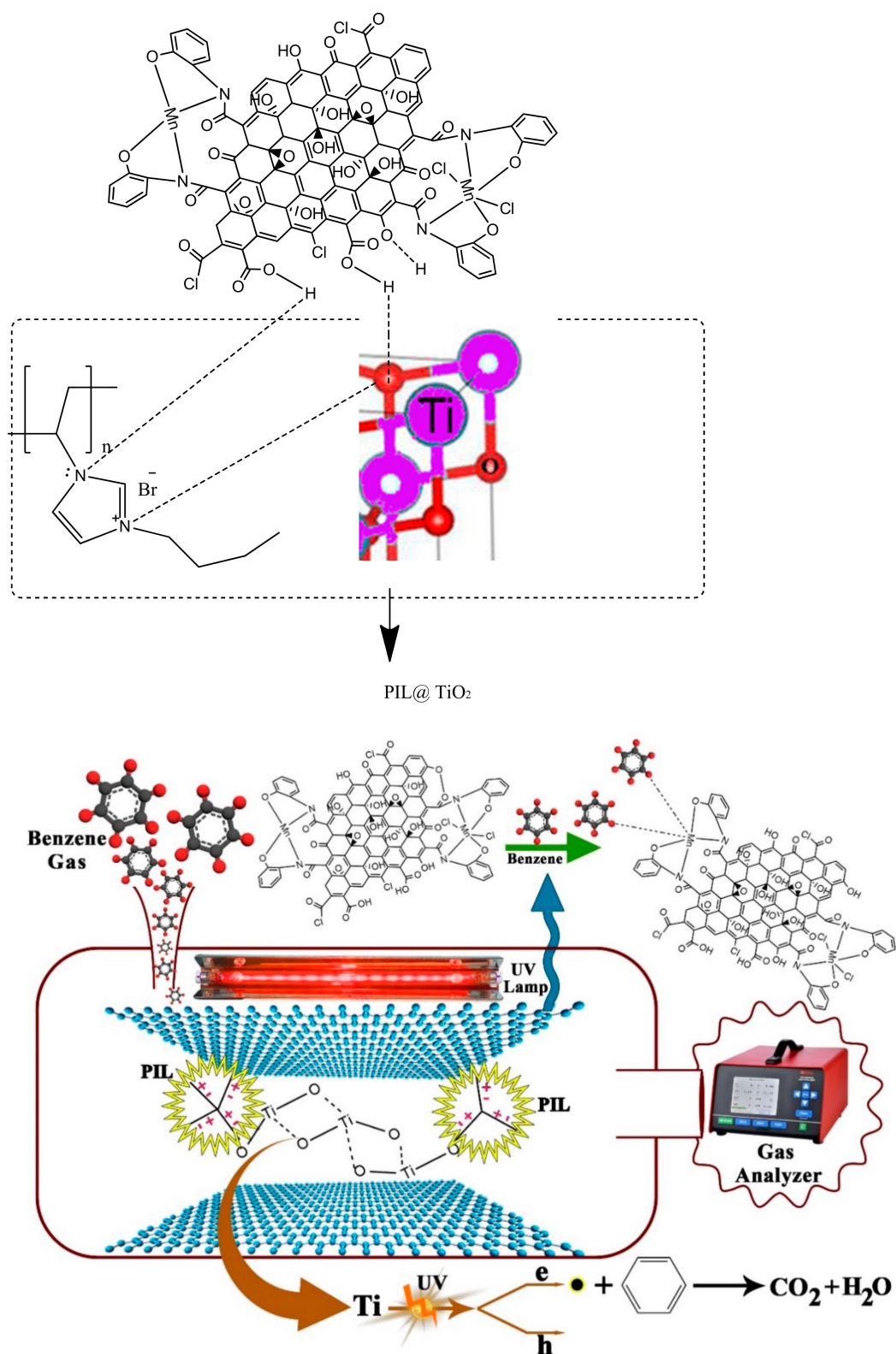


Figure 9. Schematic view of the linking PIL@TiO₂ to m-GO (top) and the absorption of benzene during the photocatalytic degradation of benzene (bottom).

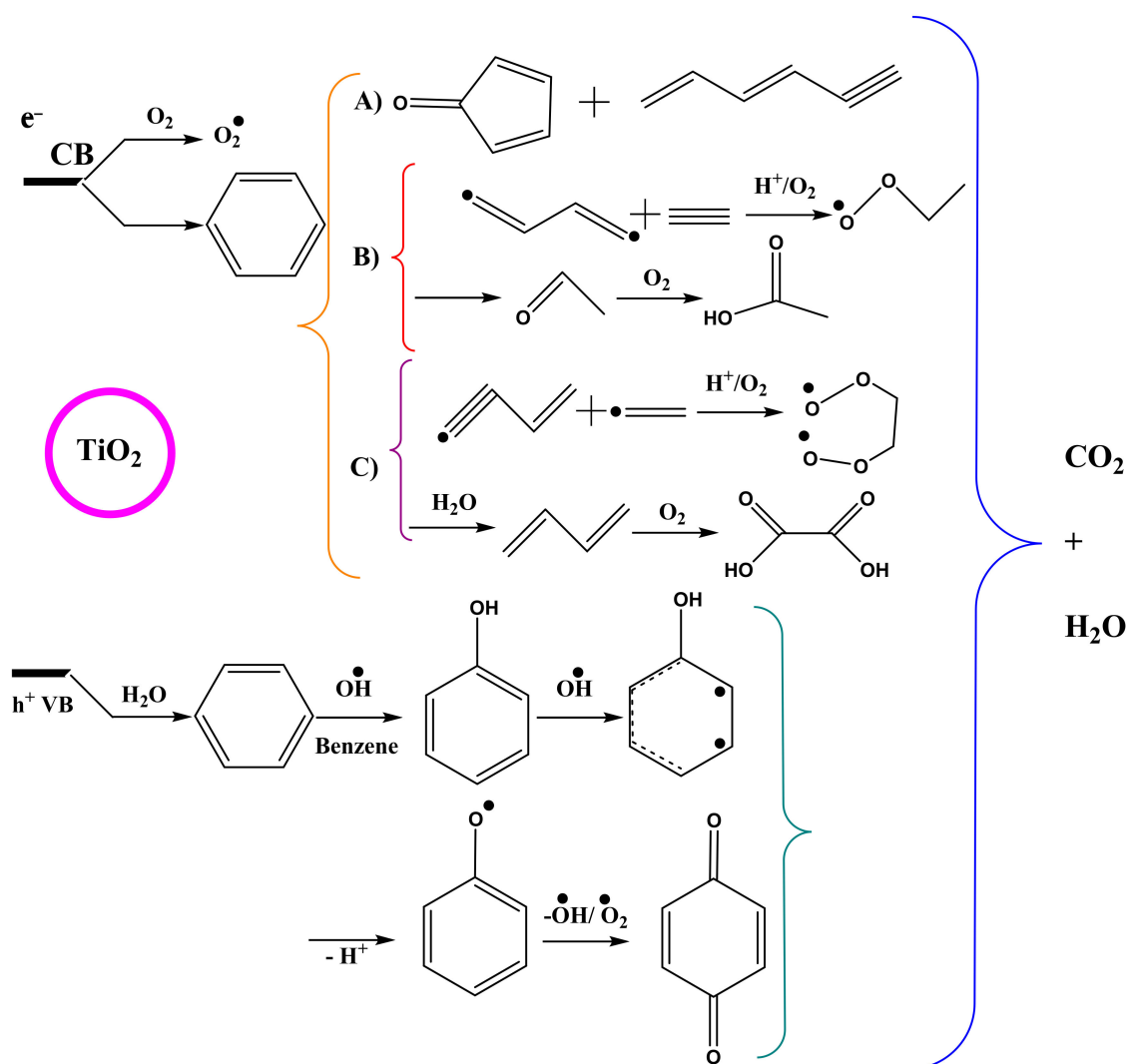


Figure 10. The mechanism of radical degradation of benzene.

The compositing of m-GO with a polyionic liquid matrix and TiO_2 exhibits the highest reduction from 3.2 eV to 2.1 eV. It means the as-prepared nanocomposite led to a bandgap downsizing and enhancing thin-film photoresponse in a remarkable area. The bandgap's narrowing can result from electronic transitions from intra-gap localized levels located above the valence band up to the conduction band. Furthermore, PIL absorbs electrons (e^- -CB) through the cation head's electrostatic interactions, and the excellent conductive characteristics of the graphene nanosheets afforded more conforming electron transportation from the conduction band, consequently withdrawing the electron-hole recombination. The separation of photogenerated electrons and holes occurs on the TiO_2 surface. Besides, the existed ions of Mn^{2+} , giving high charge density, react with the e^- -CB species as electron hunter, overcoming the electron/hole recombination [45,76,86,87].

2.3. Photocatalytic Stability

2.3.1. XRD of PIL(low)@ TiO_2 @m-GO after the Photocatalytic Reaction

By matching the two patterns, we find the photocatalyst stability of PIL(low)@ TiO_2 @mGO. As a stabilizer, the polyionic liquid chain structure performs well in maintaining the composite structure (Figure 11).

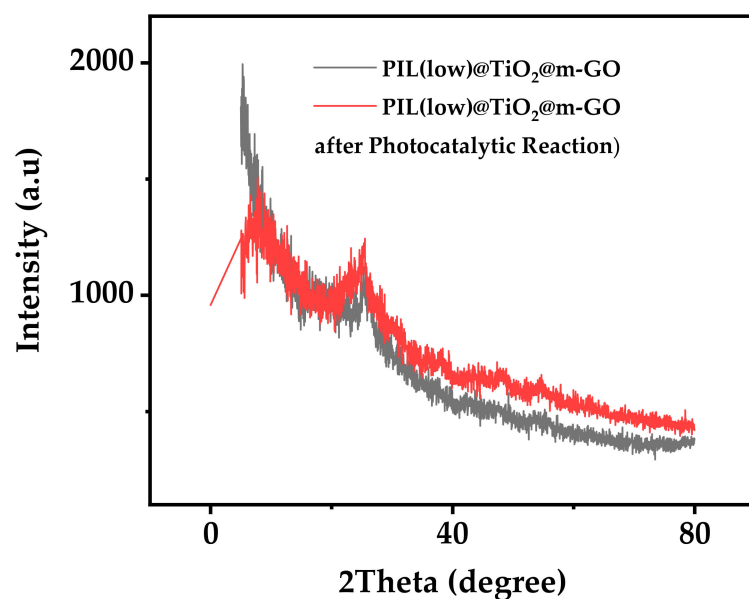


Figure 11. XRD pattern of PIL(low)@TiO₂@m-GO after the photocatalytic reaction.

2.3.2. FESEM and TEM of PIL(low)@TiO₂@m-GO after the Photocatalytic Reaction

Figure S6 shows the retention of the Composite chain structure on the graphene layers after the photocatalytic activity. Figure 12 shows the homogeneous distribution of nanoparticles on m-GO layers. This test was performed after some time to confirm the photocatalyst stability.

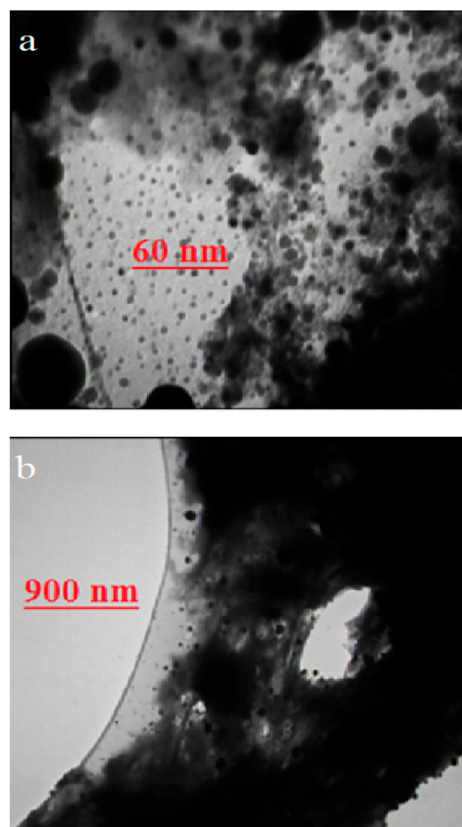


Figure 12. TEM images from different angles of PIL(low)@TiO₂@m-GO after the photocatalytic reaction, (a) 60nm magnification; (b) 900nm magnification.

2.3.3. Recycle Ability of PIL(low)/TiO₂/m-GO

The photocatalytic analysis was evaluated to determine the PIL(low)/TiO₂/m-GO nanocomposite stability during different cycles. Then, the PIL(low)/TiO₂/m-GO nanocomposite was washed with chloroform (25 mL) and dichloromethane (25 mL) at room temperature after the photocatalytic degradation analysis and followed by drying process by placing in a vacuum oven (50 °C, 24 h). Figure 13 indicates the photocatalytic stability of PIL(low)/TiO₂/m-GO for benzene and toluene degrading. The degradation rate of both pollutants in the first cycle achieved 97%. During the next rounds, the degradation efficiency was lowered, associated with photocatalyst washing or partial degradation in the photocatalyst structure [88].

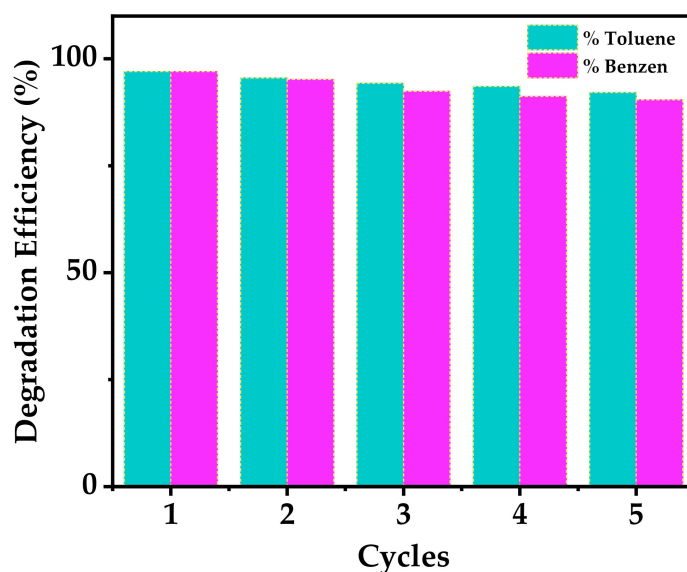


Figure 13. Recycle efficiency of PIL(low)/TiO₂/m-GO for degradation of benzene and toluene.

3. Experimental

3.1. Materials

Titanium isopropoxide Ti{OCH(CH₃)₂}₄ (M.W. 284.22 gmol⁻¹), sulfuric acid (H₂SO₄ 95%, extra pure, Merck), potassium permanganate (KMnO₄, 158.03 gmol⁻¹, extra pure; Merck), hydrogen peroxide (H₂O₂ 30%, Merck), Graphite (powder, <45_μm, ≥99.99%, Sigma-Aldrich, America), manganese (II) chloride (MnCl₂), ortho-aminophenol (C₆H₇NO), thionyl chloride (SOCl₂ 18.97 gmol⁻¹), sodium nitrate (NaNO₃ 84.99 gmol⁻¹, ≥99.0%, Merck, Germany), dilute hydrochloric acid (HCl 37% Merck diluted in H₂O, Germany), 1-vinylimidazole, 1-bromobutane, and ammonia (NH₃ 17.031 gmol⁻¹) were purchased and practiced.

3.2. Preparation and Synthesis

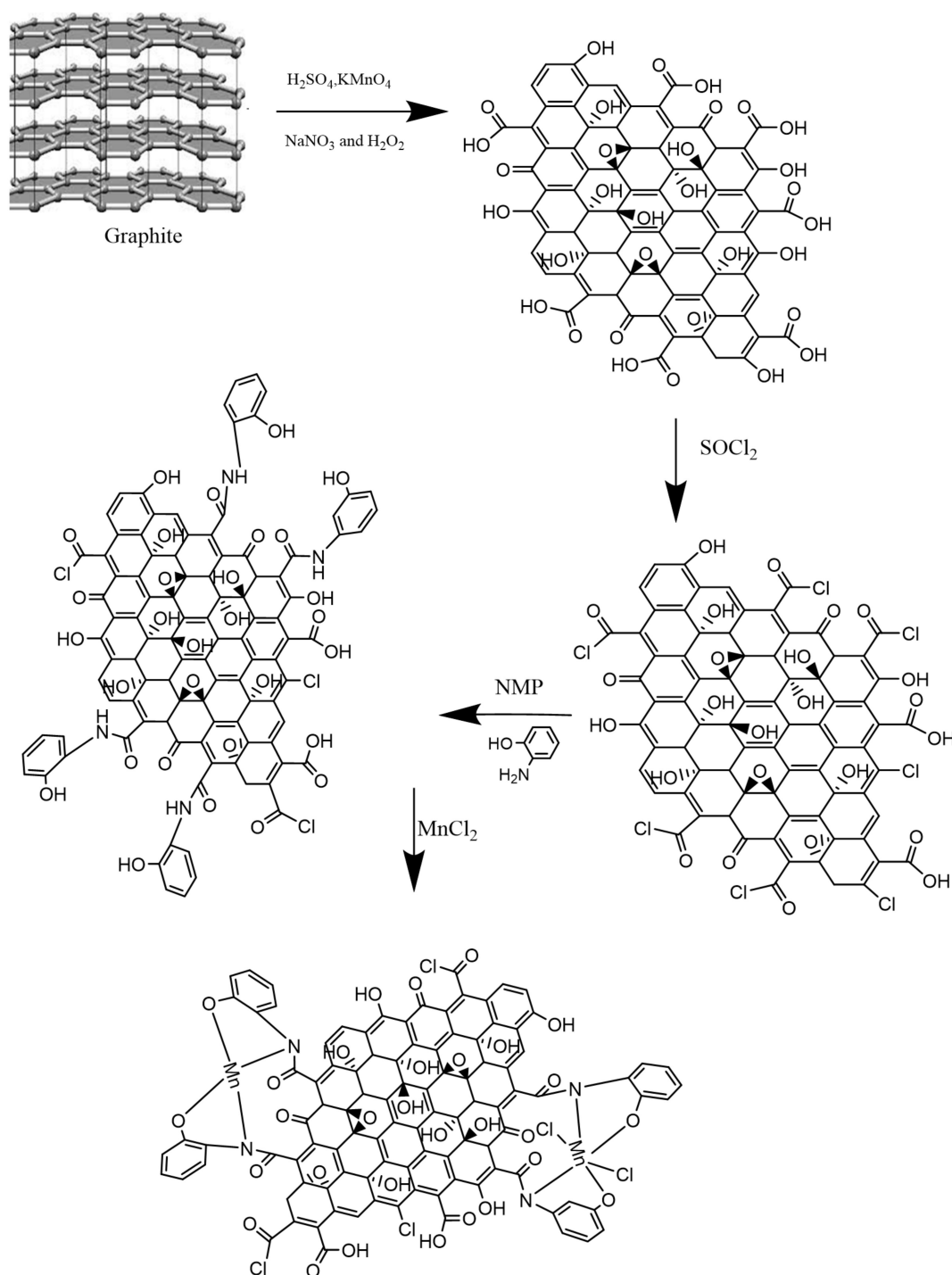
3.2.1. Preparation of Graphene Oxide (GO)

As described in the Hummer method [57,89,90], graphite (2.00 g), sodium nitrate (NaNO₃; 1 g), and H₂SO₄ (98%; 46 mL) were coupled into a flask (500 mL). Then, the mixture was stirred and simultaneously overwhelmed in an ice bath. Then, potassium permanganate (KMnO₄; 6 g) was added and gently mixed to prevent temperature exceeding 20 °C in one hour under ice bath condition. The ice bath was then removed, and the mixture's temperature increased to 35 °C in 30 min, turning brown. After half an hour, the deionized water (H₂O; 100 mL) was gently added and stirred. The sludge mixture was left at room temperature (48 h). Furthermore, hydrogen peroxide (H₂O₂; 30%; 20 mL) and warm water (300 mL) were appended to the mix-up to reduce the residual permanganate and manganese dioxide, followed by a temperature rising (98 °C). Finally, the mixture was

chilled down and washed with dilute HCl (10%), then the obtained materials dried under a vacuum [91].

3.2.2. Preparation of Modified Graphene Oxide (m-GO)

The prepared powder from previous section (GO; 5 g) was mixed with 50 mL thionyl chloride (as soluble reagent). Chlorine atoms replace with some hydroxyls of the carboxylic acid, located on the graphene oxide edge. Then, 7 g ortho amino phenol (OAP) was added in the presence of N-methyl-2-pyrrolidone (60 °C). Therefore, the OAP groups are substituted with chlorine atoms. Then, adding $MnCl_2$ led to forming, manganese functionalized graphene oxide (m-GO) (Scheme 1).



Scheme 1. The preparation procedure of manganese functionalized graphene oxide (m-GO).

3.2.3. Preparation of the Pure TiO₂

The sol–gel technique was utilized to prepare titanium dioxide (TiO₂) nanoparticles, using titanium isopropoxide (Ti{OCH(CH₃)₂}₄; 10 mL), combined with 2-propanol ((CH₃)₂CHOH, 40 mL) in a dry atmosphere. It was dropwise added into another mix-up that includes 10 mL water and 10 mL 2-propanol. Then, hydrochloric acid and ammonia were added to adjust pH = 3 and shook over an hour. Next, to evaporate the solvent's residual, a high temperature (°C) was imposed on the system. Finally, the container was placed in an oven (500 °C) for 6 h [92].

3.2.4. Preparation of 3-Butyl-1-Vinylimidazolium Bromide Monomer

Vinyl imidazole (C₅H₆N₂; 0 mmol, 0.94 g) and 1-bromobutane (CH₃(CH₂)₃Br, 10 mmol, 0.83 g) were mixed in a volumetric flask (100 mL) at lab atmosphere for 12 h under argon flow. Then, the mixture was purified using solvents.

3.2.5. Preparation of Poly 3-Butyl-1-Vinylimidazolium Bromide

A solution containing 5 mmol (0.93 g) of monomer and 11 mL of distilled water was introduced in a reactor and degassed under vacuum. Then, 14 mg of initiator 4, 4'-Azobis (4-cyanovaleric acid) (Aldrich, America, recrystallized from methanol) was added under Ar flow and magnetic stirring at 60 °C for 20 h. After cooling to room temperature, the polymer was precipitated in a mixture of water/KBr/acetone (100 mL/2.5 g/400 mL). The precipitate was recovered by filtration and washed several times with water and acetone. After drying, the polymer was purified in 10 mL of chloroform and precipitated in 200 mL of acetone. Finally, the polymer was filtered and dried under a vacuum at 50 °C for seven days.

3.2.6. Preparation of PIL@TiO₂

To compare the effect of ionic liquid and titanium dioxide ratio, we prepared two different concentrations of PIL@TiO₂. Two composites containing two different concentrations were prepared. One gram of poly[3-butyl-1-vinylimidazolium bromide] was dissolved in 20 mL ethanol (sample 1). The other mixture contained 1.8 mL titanium isopropoxide and 20 mL ethanol (sample 2). The pH was adjusted by adding 5 mL of acetic acid. By reaching a temperature of 80 °C, the mixture was stirred under a vacuum for 18 h. Residual's solvent was removed by placing the lemon-colored solution under heat. Finally, the sticky material was formed. For the second experiment, half the amount of initial ionic liquid was used. The rest steps were performed similarly to the previous item. Therefore, the less sticky powder was obtained [93].

3.3. Instrumentation

X-ray powder diffraction (XRD, X' Pert Pro model, Panalytical, The Netherland) analysis was done on an anode materials copper target. In the range of $2\theta = 5^{\circ}$ – 80° . 40 kV acceleration voltage and 40 mA applied voltage. Scanning electron microscopy (SIGMA VP model, ZEISS, Germany) was performed to verify the morphology of the sample. An accelerating voltage of 15 kV was reported. A magnification of 20–900 nm recorded transmission electron microscopy (TEM, EM10C-100 KV model, ZEISS, Germany) images of specimens. X-ray photoelectron spectroscopy (Al-K α , hv:1486.6 eV, 107 Pa, Kratos AXISUltra DLD) was reported by shining the beam X and simultaneously measuring the number of electrons released at a distance of 1 to 10 nm [76,94]. Infrared spectra (IR, Tensor 27 model, Bruker, Germany) were performed using KBr pellets. IR is a non-destructive test. An infrared spectrum represents absorption peaks associated with the vibrational frequencies between atomic bonds.

3.4. Photocatalytic Measurements

In this study, the batch reactor was used as a photocatalyst reactor. A photocatalytic thin film was placed close to the fixed UV source, including an intensity of

3.0 mW/cm² [95,96]. Photocatalytic thin-film defined a level of 50 cm². UV lamp specifications are as follows: 8 W, OSRAM, Italy. A temperature sensor was used to fix the temperature in front to the light. The assembly system was monitored concerning leakage regularly through a leaking examination in each connection. The photocatalytic outputs were prepared based on the degradation of benzene and toluene at level ppm. The analytical scale of benzene and toluene was prepared from a compressed gas with an anti-rust cylinder with a gas regulator. The relative humidity of the flow was adjusted to 40%. A mass flow controller stabilized the flow rate at 200 mL/min. Finally, benzene and toluene concentration was measured using apparatus gas chromatograph, by sampling 0.7 L/min.

4. Conclusions

In this paper, a composite structure is explained that directly degrades the pollutants under the radical mechanism, and facilitates the absorption and degradation of the complex's contaminants. PIL(low)@TiO₂/GO, degradation of 83% is shown for toluene. When graphene oxide is functionalized by manganese complexes (PIL(low)@TiO₂/m-GO), the photodegradation rate increases to 97%. Benzene degradation is another confirmation of ionic liquid and manganese complex's effect on removing pollutants, with 91% and 97% degradation reported for PIL(low)@TiO₂/GO and PIL(low)@TiO₂/m-GO, respectively. This percentage was reported within 24 min, which is a significant period.

Supplementary Materials: The following are available online at <https://www.mdpi.com/2073-4344/11/1/126/s1>.

Author Contributions: Conceptualization, S.S. and E.K.; methodology, E.K. and N.S.; software, M.D.N.; formal analysis, S.S., N.S., A.C. and G.S.; investigation, S.S., E.K., N.S. and S.R.; resources, S.S., E.K., S.R. and G.S.; writing—original draft preparation, S.S., F.B.A.; A.C.; G.S.; writing—review and editing, S.S., E.K., F.B.A., S.R., G.S., M.D.N., V.H.-A., S.A.; visualization, E.K.; supervision, E.K. All authors have read and agreed to the published version of the manuscript.

Funding: This research was funded by Amirkabir University of technology, grant number [00].

Institutional Review Board Statement: Not applicable.

Informed Consent Statement: Not applicable.

Data Availability Statement: Data is contained within the article and supplementary material.

Acknowledgments: The authors thank the Research Affairs Division at the Amir Kabir University of Technology (AUT), Tehran, Iran for their financial support.

Conflicts of Interest: The authors whose names are listed immediately below certify that they have NO affiliations with or involvement in any organization or entity with any financial interest (such as honoraria; educational grants; participation in speakers' bureaus; membership, employment, consultancies, stock ownership, or other equity interest; and expert testimony or patent-licensing arrangements), or non-financial interest (such as personal or professional relationships, affiliations, knowledge or beliefs) in the subject matter or materials discussed in this manuscript.

References

1. Khan, J.; Kakosimos, K.; Jensen, S.S.; Hertel, O.; Sørensen, M.; Gulliver, J.; Ketzler, M. The spatial relationship between traffic-related air pollution and noise in two Danish cities: Implications for health-related studies. *Sci. Total Environ.* **2020**, *726*, 138577. [[CrossRef](#)]
2. Zhang, H.; Wang, S.; Hao, J.; Wang, X.; Wang, S.; Chai, F.; Li, M. Air pollution and control action in Beijing. *J. Clean. Prod.* **2016**, *112*, 1519–1527. [[CrossRef](#)]
3. Huang, Y.; Ho, S.S.H.; Lu, Y.; Niu, R.; Xu, L.; Cao, J.; Lee, S. Removal of indoor volatile organic compounds via photocatalytic oxidation: A short review and prospect. *Molecules* **2016**, *21*, 56. [[CrossRef](#)] [[PubMed](#)]
4. Gopalan, A.-I.; Lee, J.-C.; Saianand, G.; Lee, K.-P.; Sonar, P.; Dharmarajan, R.; Hou, Y.; Ann, K.-Y.; Kannan, V.; Kim, W.-J. Recent progress in the abatement of hazardous pollutants using photocatalytic TiO₂-based building materials. *Nanomaterials* **2020**, *10*, 1854. [[CrossRef](#)] [[PubMed](#)]

5. Chen, J.; Zhang, D.; Li, G.; An, T.; Fu, J. The health risk attenuation by simultaneous elimination of atmospheric VOCs and POPs from an e-waste dismantling workshop by an integrated de-dusting with decontamination technique. *Chem. Eng. J.* **2016**, *301*, 299–305. [[CrossRef](#)]
6. Salar-García, M.J.; Ortiz-Martínez, V.M.; Hernández-Fernández, F.J.; de Los Ríos, A.P.; Quesada-Medina, J. Ionic liquid technology to recover volatile organic compounds (VOCs). *J. Hazard. Mater.* **2017**, *321*, 484–499. [[CrossRef](#)]
7. Bennett, J.W.; Inamdar, A.A. Are some fungal volatile organic compounds (VOCs) mycotoxins? *Toxins* **2015**, *7*, 3785. [[CrossRef](#)]
8. McMichael, A.J. Carcinogenicity of benzene, toluene and xylene: Epidemiological and experimental evidence. *IARC Sci. Publ.* **1988**, *85*, 3.
9. Weon, S.; Kim, J.; Choi, W. Dual-components modified TiO₂ with Pt and fluoride as deactivation-resistant photocatalyst for the degradation of volatile organic compound. *Appl. Catal. B Environ.* **2018**, *220*, 1–8. [[CrossRef](#)]
10. Liu, X.; Zhang, Y.; Matsushima, S.; Hojo, H.; Einaga, H. Photocatalytic oxidation process for treatment of gas phase benzene using Ti³⁺ self-doped TiO₂ microsphere with sea urchin-like structure. *Chem. Eng. J.* **2020**, *402*, 126220. [[CrossRef](#)]
11. Chen, R.; Zhu, C.; Lu, J.; Xiao, J.; Lei, Y.; Yu, Z. BiVO₄/α-Fe₂O₃ catalytic degradation of gaseous benzene: Preparation, characterization and photocatalytic properties. *Appl. Surf. Sci.* **2018**, *427*, 141–147. [[CrossRef](#)]
12. Wang, Q.; Rhimi, B.; Wang, H.; Wang, C. Efficient photocatalytic degradation of gaseous toluene over F-doped TiO₂/exfoliated bentonite. *Appl. Surf. Sci.* **2020**, *530*, 147286. [[CrossRef](#)]
13. Da Costa Filho, B.M.; Silva, G.V.; Boaventura, R.A.R.; Dias, M.M.; Lopes, J.C.B.; Vilar, V.J.P. Ozonation and ozone-enhanced photocatalysis for VOC removal from air streams: Process optimization, synergy and mechanism assessment. *Sci. Total Environ.* **2019**, *687*, 1357–1368. [[CrossRef](#)] [[PubMed](#)]
14. Lee, J.E.; Ok, Y.S.; Tsang, D.C.W.; Song, J.; Jung, S.-C.; Park, Y.-K. Recent advances in volatile organic compounds abatement by catalysis and catalytic hybrid processes: A critical review. *Sci. Total Environ.* **2020**, *719*, 137405. [[CrossRef](#)]
15. Han, X.; An, L.; Hu, Y.; Li, Y.; Hou, C.; Wang, H.; Zhang, Q. Ti₃C₂ MXene-derived carbon-doped TiO₂ coupled with g-C₃N₄ as the visible-light photocatalysts for photocatalytic H₂ generation. *Appl. Catal. B Environ.* **2020**, *265*, 118539. [[CrossRef](#)]
16. He, F.; Muliane, U.; Weon, S.; Choi, W. Substrate-specific mineralization and deactivation behaviors of TiO₂ as an air-cleaning photocatalyst. *Appl. Catal. B Environ.* **2020**, *275*, 119145. [[CrossRef](#)]
17. Chen, P.; Cui, W.; Wang, H.; Li, J.; Sun, Y.; Zhou, Y.; Zhang, Y.; Dong, F. The importance of intermediates ring-opening in preventing photocatalyst deactivation during toluene decomposition. *Appl. Catal. B Environ.* **2020**, *272*, 118977. [[CrossRef](#)]
18. Zhu, S.; Dong, Y.; Xia, X.; Liu, X.; Li, H. Synthesis of Mo-doped TiO₂ nanowires/reduced graphene oxide composites with enhanced photodegradation performance under visible light irradiation. *RSC Adv.* **2016**, *6*, 23809–23815. [[CrossRef](#)]
19. Xiao, W.-Z.; Xu, L.; Rong, Q.-Y.; Dai, X.-Y.; Cheng, C.-P.; Wang, L.-L. Two-dimensional H-TiO₂/MoS₂ (WS₂) van der Waals heterostructures for visible-light photocatalysis and energy conversion. *Appl. Surf. Sci.* **2020**, *504*, 144425. [[CrossRef](#)]
20. Dolat, D.; Quici, N.; Kusiak-Nejman, E.; Morawski, A.W.; Puma, G.L. One-step, hydrothermal synthesis of nitrogen, carbon co-doped titanium dioxide (N, CTiO₂) photocatalysts. Effect of alcohol degree and chain length as carbon dopant precursors on photocatalytic activity and catalyst deactivation. *Appl. Catal. B Environ.* **2012**, *115*, 81–89. [[CrossRef](#)]
21. Xu, G.; Li, M.; Wang, Y.; Zheng, N.; Yang, L.; Yu, H.; Yu, Y. A novel Ag-BiOBr-rGO photocatalyst for enhanced ketoprofen degradation: Kinetics and mechanisms. *Sci. Total Environ.* **2019**, *678*, 173–180. [[CrossRef](#)] [[PubMed](#)]
22. Su, R.; Ge, S.; Li, H.; Su, Y.; Li, Q.; Zhou, W.; Gao, B.; Yue, Q. Synchronous synthesis of Cu₂O/Cu/rGO@carbon nanomaterials photocatalysts via the sodium alginate hydrogel template method for visible light photocatalytic degradation. *Sci. Total Environ.* **2019**, *693*, 133657. [[CrossRef](#)] [[PubMed](#)]
23. Li, W.; Wang, X.; Li, M.; He, S.; Ma, Q.; Wang, X. Construction of Z-scheme and pn heterostructure: Three-dimensional porous g-C₃N₄/graphene oxide-Ag/AgBr composite for high-efficient hydrogen evolution. *Appl. Catal. B Environ.* **2020**, *268*, 118384. [[CrossRef](#)]
24. Etacheri, V.; Di Valentin, C.; Schneider, J.; Bahnemann, D.; Pillai, S.C. Visible-light activation of TiO₂ photocatalysts: Advances in theory and experiments. *J. Photochem. Photobiol. C Photochem. Rev.* **2015**, *25*, 1–29. [[CrossRef](#)]
25. Şen, B.; Akdere, E.H.; Şavk, A.; Gültekin, E.; Paralı, Ö.; Göksu, H.; Şen, F. A novel thiocarbamide functionalized graphene oxide supported bimetallic monodisperse Rh-Pt nanoparticles (RhPt/TC@GO NPs) for Knoevenagel condensation of aryl aldehydes together with malononitrile. *Appl. Catal. B Environ.* **2018**, *225*, 148–153. [[CrossRef](#)]
26. Shi, Y.-C.; Chen, S.-S.; Feng, J.-J.; Lin, X.-X.; Wang, W.; Wang, A.-J. Dicationic ionic liquid mediated fabrication of Au@Pt nanoparticles supported on reduced graphene oxide with highly catalytic activity for oxygen reduction and hydrogen evolution. *Appl. Surf. Sci.* **2018**, *441*, 438–447. [[CrossRef](#)]
27. Yuan, J.; Mecerreyes, D.; Antonietti, M. Poly(ionic liquid)s: An update. *Prog. Polym. Sci.* **2013**, *38*, 1009–1036. [[CrossRef](#)]
28. Hou, Q.; Zhen, M.; Li, W.; Liu, L.; Liu, J.; Zhang, S.; Nie, Y.; Bai, C.; Bai, X.; Ju, M. Efficient catalytic conversion of glucose into 5-hydroxymethylfurfural by aluminum oxide in ionic liquid. *Appl. Catal. B Environ.* **2019**, *253*, 1–10. [[CrossRef](#)]
29. Zhang, P.; Jiang, Z.; Cui, Y.; Xie, G.; Jin, Y.; Guo, L.; Xu, Y.; Zhang, Q.; Li, X. Catalytic performance of ionic liquid for dehydrochlorination reaction: Excellent activity and unparalleled stability. *Appl. Catal. B Environ.* **2019**, *255*, 117757. [[CrossRef](#)]
30. Qi, K.; Qi, H.; Yang, J.; Wang, G.-C.; Selvaraj, R.; Zheng, W. Experimental and theoretical DFT+D investigations regarding to various morphology of cuprous oxide nanoparticles: Growth mechanism of ionic liquid-assisted synthesis and photocatalytic activities. *Chem. Eng. J.* **2017**, *324*, 347–357. [[CrossRef](#)]

31. Wang, D.; Xu, L.; Nai, J.; Bai, X.; Sun, T. Morphology-controllable synthesis of nanocarbons and their application in advanced symmetric supercapacitor in ionic liquid electrolyte. *Appl. Surf. Sci.* **2019**, *473*, 1014–1023. [[CrossRef](#)]
32. Gai, H.; Zhong, C.; Liu, X.; Qiao, L.; Zhang, X.; Xiao, M.; Song, H. Poly (ionic liquid)-supported gold and ruthenium nanoparticles toward the catalytic wet air oxidation of ammonia to nitrogen under mild conditions. *Appl. Catal. B Environ.* **2019**, *258*, 117972. [[CrossRef](#)]
33. Huang, T.; Long, M.-C.; Wang, X.-L.; Wu, G.; Wang, Y.-Z. One-step preparation of poly (ionic liquid)-based flexible electrolytes by in-situ polymerization for dendrite-free lithium ion batteries. *Chem. Eng. J.* **2019**, *375*, 122062. [[CrossRef](#)]
34. Lee, W.G.; Kang, S.W. Highly selective poly(ethylene oxide)/ionic liquid electrolyte membranes containing CrO₃ for CO₂/N₂ separation. *Chem. Eng. J.* **2019**, *356*, 312–317. [[CrossRef](#)]
35. Liu, Y.; Wang, K.; Hou, W.; Shan, W.; Li, J.; Zhou, Y.; Wang, J. Mesoporous poly (ionic liquid) supported palladium (II) catalyst for oxidative coupling of benzene under atmospheric oxygen. *Appl. Surf. Sci.* **2018**, *427*, 575–583. [[CrossRef](#)]
36. Hummers, W.S., Jr.; Offeman, R.E. Preparation of graphitic oxide. *J. Am. Chem. Soc.* **1958**, *80*, 1339. [[CrossRef](#)]
37. Zhang, Y.; Li, Q.; Gao, Q.; Li, J.; Shen, Y.; Zhu, X. An aspirated in-syringe device fixed with ionic liquid and β -cyclodextrin-functionalized CNTs/TiO₂ for rapid adsorption and visible-light-induced photocatalytic activity. *New J. Chem.* **2019**, *43*, 9345–9353. [[CrossRef](#)]
38. Fausey, C.L.; Zucker, I.; Shaulsky, E.; Zimmerman, J.B.; Elimelech, M. Removal of arsenic with reduced graphene oxide-TiO₂-enabled nanofibrous mats. *Chem. Eng. J.* **2019**, *375*, 122040. [[CrossRef](#)]
39. Wang, M.; Hua, J.; Yang, Y. Fabrication of CDs/CdS-TiO₂ ternary nano-composites for photocatalytic degradation of benzene and toluene under visible light irradiation. *Spectrochim. Acta Part A Mol. Biomol. Spectrosc.* **2018**, *199*, 102–109. [[CrossRef](#)]
40. Lang, X.; Saianand, G.; Fu, W.; Ramakrishna, S. Photocatalytic water splitting utilizing electrospun semiconductors for solar hydrogen generation: Fabrication, Modification and Performance. *Bull. Chem. Soc. Jpn.* **2021**, *94*, 8–20. [[CrossRef](#)]
41. Lee, H.-G.; Gopalan, A.-I.; Sai-Anand, G.; Lee, B.-C.; Kang, S.-W.; Lee, K.-P. Facile synthesis of functionalized graphene-palladium nanoparticle incorporated multicomponent TiO₂ composite nanofibers. *Mater. Chem. Phys.* **2015**, *154*, 125–136. [[CrossRef](#)]
42. Ceylan, H.; Ozgit-Akgun, C.; Erkal, T.S.; Donmez, I.; Garifullin, R.; Tekinay, A.B.; Usta, H.; Biyikli, N.; Guler, M.O. Size-controlled conformal nanofabrication of biotemplated three-dimensional TiO₂ and ZnO nanonetworks. *Sci. Rep.* **2013**, *3*, 2306. [[CrossRef](#)] [[PubMed](#)]
43. Liu, Y.; Li, J.; Wang, M.; Li, Z.; Liu, H.; He, P.; Yang, X.; Li, J. Preparation and properties of nanostructure anatase TiO₂ monoliths using 1-butyl-3-methylimidazolium tetrafluoroborate room-temperature ionic liquids as template solvents. *Cryst. Growth Des.* **2005**, *5*, 1643–1649. [[CrossRef](#)]
44. Chen, H.; Nambu, A.; Wen, W.; Graciani, J.; Zhong, Z.; Hanson, J.C.; Fujita, E.; Rodriguez, J.A. Reaction of NH₃ with titania: N-doping of the oxide and TiN formation. *J. Phys. Chem. C* **2007**, *111*, 1366–1372. [[CrossRef](#)]
45. Saleem, H.; Habib, A. Study of band gap reduction of TiO₂ thin films with variation in GO contents and use of TiO₂/Graphene composite in hybrid solar cell. *J. Alloys Compd.* **2016**, *679*, 177–183. [[CrossRef](#)]
46. Freitas, R.G.; Santanna, M.A.; Pereira, E.C. Preparation and characterization of TiO₂ nanotube arrays in ionic liquid for water splitting. *Electrochim. Acta* **2014**, *136*, 404–411. [[CrossRef](#)]
47. Li, H.; Zhang, J.; Chen, X.; Pan, G.; Huo, Y. Ionic-liquid-assisted growth of flower-like TiO₂ film on Ti substrate with high photocatalytic activity. *J. Mol. Catal. A Chem.* **2013**, *373*, 12–17. [[CrossRef](#)]
48. Jana, S.; Trivedi, M.; Tallapragada, R.M.; Branton, A.; Trivedi, D.; Nayak, G.; Mishra, R.K. Characterization of physical, thermal and spectral properties of biofield treated O-aminophenol. *Pharm. Anal. Acta* **2015**, *10*. [[CrossRef](#)]
49. Qian, X.; Song, L.; Yu, B.; Yang, W.; Wang, B.; Hu, Y.; Yuen, R.K.K. One-pot surface functionalization and reduction of graphene oxide with long-chain molecules: Preparation and its enhancement on the thermal and mechanical properties of polyurea. *Chem. Eng. J.* **2014**, *236*, 233–241. [[CrossRef](#)]
50. Zhao, W.; Kido, G.; Hara, K.; Noguchi, H. Characterization of neutralized graphite oxide and its use in electric double layer capacitors. *J. Electroanal. Chem.* **2014**, *712*, 185–193. [[CrossRef](#)]
51. Ajdari, F.B.; Kowsari, E.; Ehsani, A. Ternary nanocomposites of conductive polymer/functionalized GO/MOFs: Synthesis, characterization and electrochemical performance as effective electrode materials in pseudocapacitors. *J. Solid State Chem.* **2018**, *265*, 155–166. [[CrossRef](#)]
52. Yuan, B.; Bao, C.; Song, L.; Hong, N.; Liew, K.M.; Hu, Y. Preparation of functionalized graphene oxide/polypropylene nanocomposite with significantly improved thermal stability and studies on the crystallization behavior and mechanical properties. *Chem. Eng. J.* **2014**, *237*, 411–420. [[CrossRef](#)]
53. Stobinski, L.; Lesiak, B.; Malolepszy, A.; Mazurkiewicz, M.; Mierzwa, B.; Zemek, J.; Jiricek, P.; Bieloshapka, I. Graphene oxide and reduced graphene oxide studied by the XRD, TEM and electron spectroscopy methods. *J. Electron Spectros. Relat. Phenom.* **2014**, *195*, 145–154. [[CrossRef](#)]
54. Verma, S.; Dutta, R.K. A facile method of synthesizing ammonia modified graphene oxide for efficient removal of uranyl ions from aqueous medium. *RSC Adv.* **2015**, *5*, 77192–77203. [[CrossRef](#)]
55. Yin, J.; Zhu, G.; Deng, B. Graphene oxide (GO) enhanced polyamide (PA) thin-film nanocomposite (TFN) membrane for water purification. *Desalination* **2016**, *379*, 93–101. [[CrossRef](#)]

56. Ajdari, F.B.; Kowsari, E.; Nadri, H.R.; Maghsoodi, M.; Ehsani, A.; Mahmoudi, H.; Eshkalak, S.K.; Chinnappan, A.; Jayathilak, W.; Ramakrishna, S. Electrochemical performance of Silsesquioxane-GO loaded with alkoxy substituted ammonium-based ionic liquid and POAP for supercapacitor. *Electrochim. Acta* **2020**, *354*, 136663. [[CrossRef](#)]
57. Ashtiani, A.A.; Kowsari, E.; Haddadi-Asl, V.; Yousefi, M.; Naderi, H.R.; Chinnappan, A.; Ramakrishna, S. Pseudocapacitive efficiency of covalently Cr-complex with L-histidine-methyl ester as a ligand graphene oxide blended with conducting polymer (POAP) as electrode material in supercapacitor. *J. Mol. Liq.* **2020**, *315*, 113697. [[CrossRef](#)]
58. Eshlaghi, M.A.; Kowsari, E.; Ehsani, A.; Akbari-Adergani, B.; Hekmati, M. Functionalized graphene oxide GO-[imi-(CH₂)₂-NH₂] as a high efficient material for electrochemical sensing of lead: Synthesis surface and electrochemical characterization. *J. Electroanal. Chem.* **2020**, *858*, 113784. [[CrossRef](#)]
59. Takehira, H.; Karim, M.R.; Shudo, Y.; Fukuda, M.; Mashimo, T.; Hayami, S. Modulating the Work Function of Graphene by Pulsed Plasma Aided Controlled Chlorination. *Sci. Rep.* **2018**, *8*, 1–8. [[CrossRef](#)]
60. Kowsari, E.; Morad, F.; Seifvand, N.; Bazri, B.; Karimi, M. Synthesis of reduced graphene oxide functionalized with methyl red dye and its role in enhancing photoactivity in TiO₂-IL/WO₃ composite for toluene degradation. *Res. Chem. Intermed.* **2020**, *46*, 1217–1234. [[CrossRef](#)]
61. Wei, H.; Ma, Y.; Luo, J.; Wu, K.-H.; Xie, W.; Wen, G.; Chiang, C.-L.; Yan, W.; Perathoner, S.; Centi, G. Creation of N-C=O active groups on N-doped CNT as an efficient CarboCatalyst for solvent-free aerobic coupling of benzylamine. *Carbon* **2020**, *170*, 338–346. [[CrossRef](#)]
62. Sivarajini, B.; Mangaiyarkarasi, R.; Ganesh, V.; Umadevi, S. Vertical alignment of liquid crystals over a functionalized flexible substrate. *Sci. Rep.* **2018**, *8*, 1–13. [[CrossRef](#)] [[PubMed](#)]
63. Mao, L.; Zhang, K.; Chan, H.S.O.; Wu, J. Nanostructured MnO₂/graphene composites for supercapacitor electrodes: The effect of morphology, crystallinity and composition. *J. Mater. Chem.* **2012**, *22*, 1845–1851. [[CrossRef](#)]
64. Fu, Y.; Wei, Q.; Zhang, G.; Wang, X.; Zhang, J.; Hu, Y.; Wang, D.; Zuin, L.; Zhou, T.; Wu, Y. High-Performance Reversible Aqueous Zn-Ion Battery Based on Porous MnOx Nanorods Coated by MOF-Derived N-Doped Carbon. *Adv. Energy Mater.* **2018**, *8*, 1801445. [[CrossRef](#)]
65. Sivachandiran, L.; Khacef, A. Enhanced seed germination and plant growth by atmospheric pressure cold air plasma: Combined effect of seed and water treatment. *RSC Adv.* **2017**, *7*, 1822–1832. [[CrossRef](#)]
66. Ehsani, A.; Kowsari, E.; Boorboor Ajdari, F.; Safari, R.; Mohammad Shiri, H. Influence of newly synthesized geminal dicationic ionic liquid on electrochemical and pseudocapacitance performance of conductive polymer electroactive film. *J. Colloid Interface Sci.* **2017**, *505*, 1158–1164. [[CrossRef](#)]
67. Ehsani, A.; Kowsari, E.; Boorboor Ajdari, F.; Safari, R.; Mohammad Shiri, H. Sulfonated graphene oxide and its nanocomposites with electroactive conjugated polymer as effective pseudocapacitor electrode materials. *J. Colloid Interface Sci.* **2017**, *497*, 258–265. [[CrossRef](#)]
68. Ajdari, F.B.; Kowsari, E.; Ehsani, A.; Schorowski, M.; Ameri, T. New synthesized ionic liquid functionalized graphene oxide: Synthesis, characterization and its nanocomposite with conjugated polymer as effective electrode materials in an energy storage device. *Electrochim. Acta* **2018**, *292*, 789–804. [[CrossRef](#)]
69. Vahur, S.; Kriiska, A.; Leito, I. Investigation of the adhesive residue on the flint insert and the adhesive lump found from the Pulli Early Mesolithic settlement site (Estonia) by micro-ATR-FT-IR spectroscopy. *Est. J. Archaeol.* **2011**, *15*, 3. [[CrossRef](#)]
70. Hassan, S.; Suzuki, M.; El-Moneim, A.A. Facile synthesis of MnO₂/graphene electrode by two-steps electrodeposition for energy storage application. *Int. J. Electrochem. Sci.* **2014**, *9*, 8340–8354.
71. How, G.T.S.; Pandikumar, A.; Ming, H.N.; Ngee, L.H. Highly exposed {001} facets of titanium dioxide modified with reduced graphene oxide for dopamine sensing. *Sci. Rep.* **2014**, *4*, 5044. [[CrossRef](#)] [[PubMed](#)]
72. Veerapandian, M.; Seo, Y.-T.; Yun, K.; Lee, M.-H. Graphene oxide functionalized with silver@silica-polyethylene glycol hybrid nanoparticles for direct electrochemical detection of quercetin. *Biosens. Bioelectron.* **2014**, *58*, 200–204. [[CrossRef](#)] [[PubMed](#)]
73. Gong, Y.; Li, D.; Fu, Q.; Pan, C. Influence of graphene microstructures on electrochemical performance for supercapacitors. *Prog. Nat. Sci. Mater. Int.* **2015**, *25*, 379–385. [[CrossRef](#)]
74. Rudolph, W.W.; Irmer, G. Hydration and speciation studies of Mn²⁺ in aqueous solution with simple monovalent anions (ClO⁴⁻, NO³⁻, Cl⁻, Br⁻). *Dalt. Trans.* **2013**, *42*, 14460–14472. [[CrossRef](#)] [[PubMed](#)]
75. He, F.; Ma, F.; Li, T.; Li, G. Solvothermal synthesis of N-doped TiO₂ nanoparticles using different nitrogen sources, and their photocatalytic activity for degradation of benzene. *Chin. J. Catal.* **2013**, *34*, 2263–2270. [[CrossRef](#)]
76. Seifvand, N.; Kowsari, E. TiO₂/in-situ reduced GO/functionalized with an IL-Cr complex as a ternary photocatalyst composite for efficient carbon monoxide deterioration from air. *Appl. Catal. B Environ.* **2017**, *206*, 184–193. [[CrossRef](#)]
77. Li, F.B.; Li, X.Z.; Ao, C.H.; Lee, S.C.; Hou, M.F. Enhanced photocatalytic degradation of VOCs using Ln³⁺-TiO₂ catalysts for indoor air purification. *Chemosphere* **2005**, *59*, 787–800. [[CrossRef](#)]
78. Huang, J.; Wang, X.; Hou, Y.; Chen, X.; Wu, L.; Fu, X. Degradation of benzene over a zinc germanate photocatalyst under ambient conditions. *Environ. Sci. Technol.* **2008**, *42*, 7387–7391. [[CrossRef](#)]
79. Liang, Y.; Liu, Y.; Deng, J.; Zhang, K.; Hou, Z.; Zhao, X.; Zhang, X.; Zhang, K.; Wei, R.; Dai, H. Coupled Palladium-Tungsten Bimetallic Nanosheets/TiO₂ Hybrids with Enhanced Catalytic Activity and Stability for the Oxidative Removal of Benzene. *Environ. Sci. Technol.* **2019**, *53*, 5926–5935. [[CrossRef](#)]

80. Zhong, J.; Wang, J.; Tao, L.; Gong, M.; Zhimin, L.; Chen, Y. Photocatalytic degradation of gaseous benzene over $\text{TiO}_2/\text{Sr}_2\text{CeO}_4$: Kinetic model and degradation mechanisms. *J. Hazard. Mater.* **2007**, *139*, 323–331. [[CrossRef](#)]
81. Ma, J.; Zhu, C.; Xu, Y.; Lu, J.; Huang, L.; Yang, Z. Photocatalytic degradation of gaseous benzene with $\text{H}_3\text{PW}_{12}\text{O}_{40}/\text{TiO}_2$ /palygorskite composite catalyst. *J. Saudi Chem. Soc.* **2017**, *21*, 132–142. [[CrossRef](#)]
82. Liu, G.; Huang, H.; Xie, R.; Feng, Q.; Fang, R.; Shu, Y.; Zhan, Y.; Ye, X.; Zhong, C. Enhanced degradation of gaseous benzene by a Fenton reaction. *RSC Adv.* **2016**, *7*, 71–76. [[CrossRef](#)]
83. Kask, M.; Bolobajev, J.; Krichevskaya, M. Gas-phase photocatalytic degradation of acetone and toluene, and their mixture in the presence of ozone in continuous multi-section reactor as possible air post-treatment for exhaust from pulsed corona discharge. *Chem. Eng. J.* **2020**, *399*, 125815. [[CrossRef](#)]
84. Abe, R.; Sayama, K.; Domen, K.; Arakawa, H. A new type of water splitting system composed of two different TiO_2 photocatalysts (anatase, rutile) and a IO_3^-/I^- shuttle redox mediator. *Chem. Phys. Lett.* **2001**, *344*, 339–344. [[CrossRef](#)]
85. Abe, A.; Yamashita, K. Theoretical study on the photo-stimulated desorption of Xe from an oxidized Si (0 0 1) surface. *Chem. Phys. Lett.* **2001**, *343*, 143–150. [[CrossRef](#)]
86. Ghasemi, S.; Setayesh, S.R.; Habibi-Yangjeh, A.; Hormozi-Nezhad, M.R.; Gholami, M.R. Assembly of $\text{CeO}_2\text{-TiO}_2$ nanoparticles prepared in room temperature ionic liquid on graphene nanosheets for photocatalytic degradation of pollutants. *J. Hazard. Mater.* **2012**, *199–200*, 170–178. [[CrossRef](#)]
87. Chávez, A.M.; Solís, R.R.; Beltrán, F.J. Magnetic graphene TiO_2 -based photocatalyst for the removal of pollutants of emerging concern in water by simulated sunlight aided photocatalytic ozonation. *Appl. Catal. B Environ.* **2020**, *262*, 118275. [[CrossRef](#)]
88. Kim, J.; Lee, B.-K. Enhanced photocatalytic decomposition of VOCs by visible-driven photocatalyst combined Cu- TiO_2 and activated carbon fiber. *Process Saf. Environ. Prot.* **2018**, *119*, 164–171. [[CrossRef](#)]
89. Shoushtarian, F.; Moghaddam, M.R.A.; Kowsari, E. Efficient regeneration/reuse of graphene oxide as a nanoadsorbent for removing basic Red 46 from aqueous solutions. *J. Mol. Liq.* **2020**, *312*, 113386. [[CrossRef](#)]
90. Zaaba, N.I.; Foo, K.L.; Hashim, U.; Tan, S.J.; Liu, W.-W.; Voon, C.H. Synthesis of Graphene Oxide using Modified Hummers Method: Solvent Influence. *Procedia Eng.* **2017**, *184*, 469–477. [[CrossRef](#)]
91. Karami, A. Synthesis of TiO_2 nano powder by the sol-gel method and its use as a photocatalyst. *J. Iran. Chem. Soc.* **2010**, *7*, S154–S160. [[CrossRef](#)]
92. Zhang, L.; Du, J.; Ran, T.; Gao, H.; Liao, Y. Preparation and application of poly (zwitterionic ionic liquid) to enhance the photocatalytic activity of TiO_2 . *J. Mater. Sci.* **2016**, *51*, 7186–7198. [[CrossRef](#)]
93. Meinke, W.W.; Taylor, J.K. *Analytical Chemistry: Key to Progress on National Problems: Proceedings*; National Bureau of Standards: Washington, DC, USA, 1972; Volume 13.
94. Suryanarayana, C.; Grant, N.M. *X-Ray Diffraction—A Practical Approach*; Plenum Press: New York, NY, USA, 1998.
95. Lee, J.-C.; Gopalan, A.-I.; Saianand, G.; Lee, K.-P.; Kim, W.-J. Manganese and Graphene Included Titanium Dioxide Composite Nanowires: Fabrication, Characterization and Enhanced Photocatalytic Activities. *Nanomaterials* **2020**, *10*, 456. [[CrossRef](#)] [[PubMed](#)]
96. Lee, J.-C.; Gopalan, A.-I.; Sai-Anand, G.; Lee, K.-P.; Kim, W.-J. Preparation of visible light photocatalytic graphene embedded rutile titanium (IV) oxide composite nanowires and enhanced NO_x removal. *Catalysts* **2019**, *9*, 170. [[CrossRef](#)]